



HAL
open science

Western Mediterranean Sea Paleothermometry Over the Last Glacial Cycle Based on the Novel RI-OH Index

Nina Davtian, Guillemette Ménot, Yoann Fagault, Edouard Bard

► **To cite this version:**

Nina Davtian, Guillemette Ménot, Yoann Fagault, Edouard Bard. Western Mediterranean Sea Paleothermometry Over the Last Glacial Cycle Based on the Novel RI-OH Index. *Paleoceanography and Paleoclimatology*, 2019, 34 (4), pp.616 - 634. 10.1029/2018PA003452 . hal-02115659

HAL Id: hal-02115659

<https://hal.science/hal-02115659>

Submitted on 1 Sep 2021

HAL is a multi-disciplinary open access archive for the deposit and dissemination of scientific research documents, whether they are published or not. The documents may come from teaching and research institutions in France or abroad, or from public or private research centers.

L'archive ouverte pluridisciplinaire **HAL**, est destinée au dépôt et à la diffusion de documents scientifiques de niveau recherche, publiés ou non, émanant des établissements d'enseignement et de recherche français ou étrangers, des laboratoires publics ou privés.

Copyright

Paleoceanography and Paleoclimatology

RESEARCH ARTICLE

10.1029/2018PA003452

Key Points:

- RI-OH consistently records glacial-interglacial transitions and abrupt climatic events despite substantial terrigenous inputs
- RI-OH could reflect winter and/or subsurface temperatures rather than annual sea surface temperatures in the Gulf of Lions
- RI-OH-based interglacial-glacial anomalies are high but plausible compared to reported anomalies in the western Mediterranean Sea

Supporting Information:

- Supporting Information S1
- Data Set S1
- Data Set S2
- Data Set S3

Correspondence to:

N. Davtian,
davtian@cerege.fr

Citation:

Davtian, N., Ménot, G., Fagault, Y., & Bard, E. (2019). Western Mediterranean Sea paleothermometry over the last glacial cycle based on the novel RI-OH index. *Paleoceanography and Paleoclimatology*, 34, 616–634. <https://doi.org/10.1029/2018PA003452>




Received 1 AUG 2018

Accepted 22 MAR 2019

Accepted article online 28 MAR 2019

Published online 29 APR 2019

Western Mediterranean Sea Paleothermometry Over the Last Glacial Cycle Based on the Novel RI-OH Index

Nina Davtian¹ , Guillemette Ménot², Yoann Fagault¹ , and Edouard Bard¹ 

¹CEREGE, Aix-Marseille University, CNRS, IRD, INRA, Collège de France, Technopôle de l'Arbois, Aix-en-Provence, France, ²Univ Lyon, ENS de Lyon, Université Lyon 1, CNRS, UMR 5276 LGL-TPE, Lyon, France

Abstract RI-OH (ring index of hydroxylated tetraethers) has recently been proposed to reconstruct paleotemperatures in middle- to low-latitude marginal seas. However, RI-OH has barely been tested in marginal seas under substantial terrigenous inputs. Here we analyze tetraether lipids in two adjacent marine cores from the Gulf of Lions. We then test for the first time the RI-OH paleothermometer from 160 to 9 ka BP in the western Mediterranean Sea. While terrigenous inputs prevent TEX₈₆ (TetraEther indeX of tetraethers consisting of 86 carbon atoms) from behaving as a paleothermometer, RI-OH is generally consistent with other paleothermometric proxies. RI-OH also responds systematically and coherently to glacial-interglacial transitions as well as to abrupt climatic events. The average difference between RI-OH temperatures and November–May U^{K'}₃₇ (C₃₇ ketone unsaturation ratio) temperatures is -2.0 °C with a standard error of 0.4 °C based on 249 RI-OH-U^{K'}₃₇ comparisons. This systematic difference suggests that hydroxylated tetraethers and alkenones record different temperatures, for instance, winter and/or subsurface temperatures for RI-OH. Another source of bias could be linked to the available RI-OH-temperature calibration, which clearly needs more work at the global and regional scales, notably for semienclined basins such as the Mediterranean Sea. Nevertheless, our RI-OH-based interglacial-glacial anomalies are of 10 °C, a value within the high end of anomalies from previously published temperature records in the western Mediterranean Sea (from 3 to 13 °C). The RI-OH-based temperature anomalies also confirm the regional differences and seasonal contrasts in interglacial-glacial anomalies produced by models.

1. Introduction

U^{K'}₃₇ (C₃₇ ketone unsaturation ratio) and TEX₈₆ (TetraEther indeX of tetraethers consisting of 86 carbon atoms) are the most widely used organic paleothermometric proxies. U^{K'}₃₇ is based on alkenones produced by Haptophyte algae (Prahl & Wakeham, 1987). TEX₈₆ is based on nonhydroxylated isoprenoid glycerol dialkyl glycerol tetraethers (iGDGTs) produced by ammonia oxidizing *Thaumarchaeota* (Schouten et al., 2002). U^{K'}₃₇ and TEX₈₆ values increase with temperature due to decreased alkenone unsaturation and increased iGDGT cyclization, respectively (e.g., Kim et al., 2010; Müller et al., 1998; Prahl & Wakeham, 1987; Schouten et al., 2002; Tierney & Tingley, 2015, 2018). However, nutrient availability, lateral transport, and differential degradation can bias U^{K'}₃₇ values (e.g., Kim et al., 2009; Prahl et al., 2003; Rontani et al., 2013; Sikes et al., 2005). Similarly, inputs of terrestrial iGDGTs, methanotrophic interferences, and iGDGT production in subsurface waters can bias TEX₈₆ values (e.g., Ho et al., 2014; Huguet et al., 2007; Kim et al., 2015, 2016; Taylor et al., 2013; Weijers et al., 2006; Zhang et al., 2011). Seasonal biases are also to be considered for U^{K'}₃₇ and TEX₈₆ (e.g., Rosell-Melé & Prahl, 2013; Schouten et al., 2013, and references therein; Tierney & Tingley, 2014, 2018).

Lü et al. (2015) have recently developed RI-OH (ring index of hydroxylated tetraethers) in middle- to low-latitude marginal seas under substantial terrigenous inputs. RI-OH is based on hydroxylated isoprenoid glycerol dialkyl glycerol tetraethers (OH-GDGTs) produced by ammonia oxidizing Group I.1a *Thaumarchaeota* (Elling et al., 2014, 2015, 2017; Liu et al., 2012; Sinninghe Damsté et al., 2012). Below 25 °C, RI-OH values increase with temperature due to increased OH-GDGT cyclization (Lü et al., 2015; Yang et al., 2018; Zhu et al., 2016). Lü et al. (2015) have also developed RI-OH', which is an alternative version of RI-OH for temperature estimates in polar oceans. To date, de Bar et al. (2019) and Kremer et al. (2018) alone have used RI-OH and RI-OH', respectively. In addition, only a few studies have assessed potential biases for RI-OH and RI-OH', such as inputs of terrestrial OH-GDGTs, seasonal biases, and OH-GDGT production in subsurface waters (Kang et al., 2017; Lü et al., 2015, 2019; Yang et al., 2019; Zhu et al., 2016).

In this study, we present one of the first RI-OH-based sea surface temperature (SST) records covering the 160–9 ka BP period from two adjacent marine cores located in the Gulf of Lions (western Mediterranean Sea) using the global calibration proposed by Lü et al. (2015). Using independent paleothermometric proxies, including $U^{K'}_{37}$ (Cortina et al., 2015), we assess the validity of the new RI-OH record and corresponding SST estimates. We then compare the interglacial-glacial SST anomalies from the study site with a multiproxy selection of marine sites from the Iberian Margin, the Gulf of Cadiz, and the western Mediterranean Sea, including the Siculo-Tunisian Strait. In addition, we have used several models to complement our regional comparison of interglacial-glacial SST anomalies.

The Gulf of Lions constitutes a test bench for GDGT-based paleothermometers since it has planktic $\delta^{18}O$ and $U^{K'}_{37}$ -based temperature records covering the last glacial cycle (Cortina et al., 2015; Sierro et al., 2009), which helps to assess whether RI-OH behaves as a better paleothermometer than TEX_{86} during the last glacial cycle. Furthermore, the peculiar setting of the Gulf of Lions allows to test the relevance of the global calibration by Lü et al. (2015) in the semienclosed Mediterranean Sea, and in a prodelta that received substantial terrigenous inputs during the partial emersions (Frigola et al., 2012; Sierro et al., 2009).

2. Study Area

The study site is located in the upper slope of the Gulf of Lions, which is itself located in the northwestern part of the Mediterranean Sea (Figure 1). The Northern Current is the main driver of hydrodynamics in the Gulf of Lions and is divided into two branches which describe a cyclonic circulation: the main branch flows along the continental slope, whereas the secondary branch penetrates onto the continental shelf (Figure 1; Millot, 1990). The Gulf of Lions is also a major source of deep waters in the Mediterranean Sea due to the strong influence of northwesterly winds, especially in winter (Figures 1 and 2a; MEDOC GROUP, 1970; Pinardi & Masetti, 2000). The northwesterly winds induce upwelling of cold waters (Millot, 1990), resulting in SSTs of 13 to 21 °C in February and July, respectively (Figure 2b; Locarnini et al., 2013). The northwesterly winds also induce deep convection in the western Mediterranean Sea, which amplifies algal blooms in late winter-early spring and subsequent primary productivity throughout the water column (Figure 2c; Bosc et al., 2004; D'Ortenzio et al., 2014).

The water column in the Gulf of Lions is homogenous from January to March with a temperature of roughly 13–14 °C (Figure 2b). Then, the northwesterly winds weaken (Figure 2a) and the water column stratifies until September with a maximum temperature difference of 8 °C between the surface and the bottom of the thermocline at 100 m (Figure 2b). Following this, the northwesterly winds strengthen (Figure 2a) and mixing occurs from October to December (Figure 2b). Temperatures at 50 m slowly increase from February to October, peaking at 16.5 °C in November, before decreasing back to 13–14 °C (Figure 2b). Temperatures at water depths of 100 m and below are 13–14 °C year-round (Figure 2b).

The seasonal thermocline (Figure 2b) as well as stronger northwesterly winds (Figure 2a) and high lithogenic fluxes in autumn-winter bring more nutrients to surface waters (Cruzado & Velasquez, 1990; Monaco et al., 1990), leading to primary productivity peaks in March, which decrease progressively until December (Figure 2c; Bosc et al., 2004). The peak in primary productivity corresponds to late winter-early spring siliceous and calcareous phytoplankton blooms (Monaco et al., 1990; Rigual-Hernández et al., 2013), which are followed by maximal alkenone fluxes in April–June and September–November (Figure 2c; Sicre et al., 1999; Ternois et al., 1996, 1997). The 0- to 50-m depth-weighted average temperature is 15.5 °C when weighted by primary productivity and 16.4 °C when weighted by the two maxima of alkenone fluxes (Figure 2b). The 0- to 200-m depth-weighted average temperature is 13.9 °C when weighted by primary productivity and 13.7 °C when weighted by the maximum of lithogenic fluxes (Figure 2b).

3. Materials and Methods

3.1. Core Sediments and Age Model

We studied a composite sedimentary record of two marine archives from the Gulf of Lions at a water depth of 298 m (42.690°N, 3.838°E), core MD99-2348, and borehole PRGL1-4 (Figure 1). Core MD99-2348 was retrieved from the interfluvial of the Bourcart/Aude and Hérault canyons during the IMAGES V cruise of R/V Marion Dufresne. The core consists of roughly 22 m of fine-grained sediment (silty clay) with a

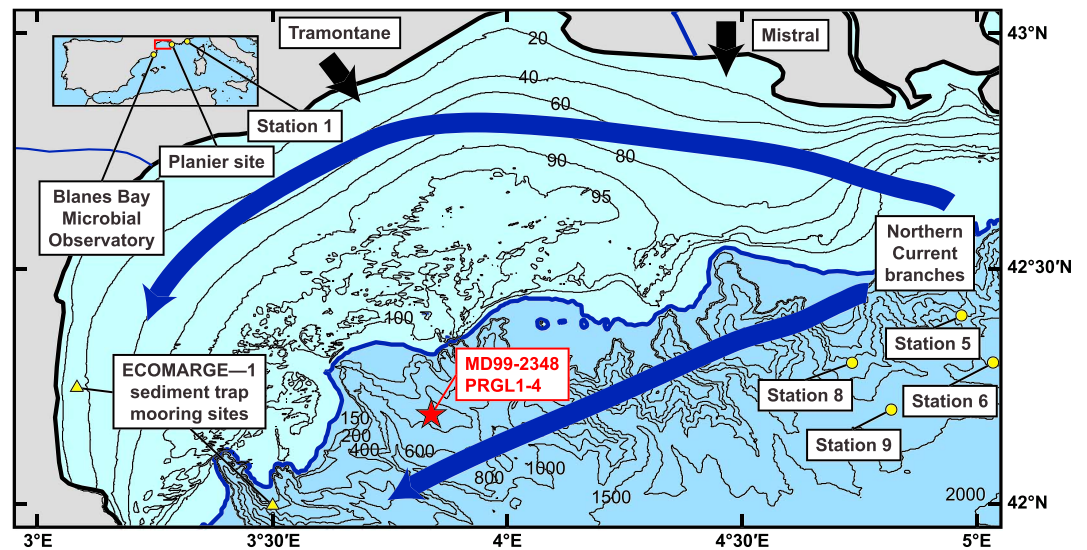


Figure 1. Location of the MD99-2348/PRGL1-4 study site within the Gulf of Lions and western Mediterranean Sea. The branches of the Northern Current and dominant northwesterly winds are shown. The other located sites are ECOMARGE—1 sediment trap mooring sites (Monaco et al., 1990), Stations 5, 6, 8, and 9 (Cacho, Pelejero, et al., 1999), Station 1 (Sicre et al., 1999; Ternois et al., 1996, 1997), Blanes Bay Microbial Observatory, Catalonia, Spain (Galand et al., 2010), and the Planier submarine canyon (Rigual-Hernández et al., 2013). The glacial maxima coastline (assuming lowstands with a relative sea level of -120 m; Zickel et al., 2016) is also shown.

20-cm-thick sandy layer at the top. Borehole PRGL1-4 was retrieved in 2004 from the same site as core MD99-2348 in the framework of the European Union project PROMESS1 (PROfiles across Mediterranean Sedimentary Systems). The borehole is 300-m long and essentially consists of fine grained sediments with several interbedded centimeter-thick sandy layers. Our study focuses on the entire core MD99-2348 and the 19–110 m below sea floor (mbsf) depth interval of borehole PRGL1-4, which corresponds to the 160–9 ka BP period.

We used the published age models by Sierro et al. (2009) and Frigola et al. (2012), established for core MD99-2348 and borehole PRGL1-4. For the last 120 ka, the composite MD99-2348/PRGL1-4 records of *Globigerina bulloides* $\delta^{18}\text{O}$ and abundance of temperate-to-warm planktic foraminifers were synchronized to the North Greenland Ice Core Project (NGRIP) ice core isotopes in Greenland (Andersen et al., 2006; North Greenland Ice Core Project members, 2004; Rasmussen et al., 2006; Svensson et al., 2008). From 120 ka BP—the age of the oldest NGRIP data—to the end of borehole PRGL1-4, the PRGL1-4 record of *Globigerina bulloides* $\delta^{18}\text{O}$ was mainly synchronized to the LR04 benthic isotope stack (Lisiecki & Raymo, 2005).

3.2. Sample Preparation and GDGT Analysis

We took 135 and 290 sediment samples from core MD99-2348 and borehole PRGL1-4, respectively. We took the sediment samples at 18- to 45-cm averaged intervals from both marine archives, except the 20 first cm of MD99-2348 and the 63–73 mbsf depth interval of PRGL1-4, from which we took the sediments samples at 2- and 13-cm averaged intervals, respectively (see Table S1 in the supporting information for more details). We then freeze dried the sediment samples before grinding and homogenization.

We extracted roughly 2.5–3.0 g of each sediment sample with dichloromethane (DCM):methanol (9:1, v:v) using an accelerated solvent extractor ASE 350 (Dionex) at 120 °C and 10^7 Pa at CEREGE. Total lipid extracts were then separated following the automated procedure established by Sanchi et al. (2013). In short, we used the TRILUTION™ LH software to operate a Gilson GX-271 ASPEC™ system. Prepacked Sigma-Aldrich® cartridges (Supelclean™ LC-Alumina-B 1 g/3 ml) were conditioned with 3 ml of hexane:DCM (1:1, v:v) before receiving the samples dissolved in 0.5 ml of the same solvent. Then, apolar and polar fractions were obtained by eluting 3.5 ml of hexane:DCM (1:1, v:v) and 5 ml of methanol:DCM (1:1, v:v), respectively.

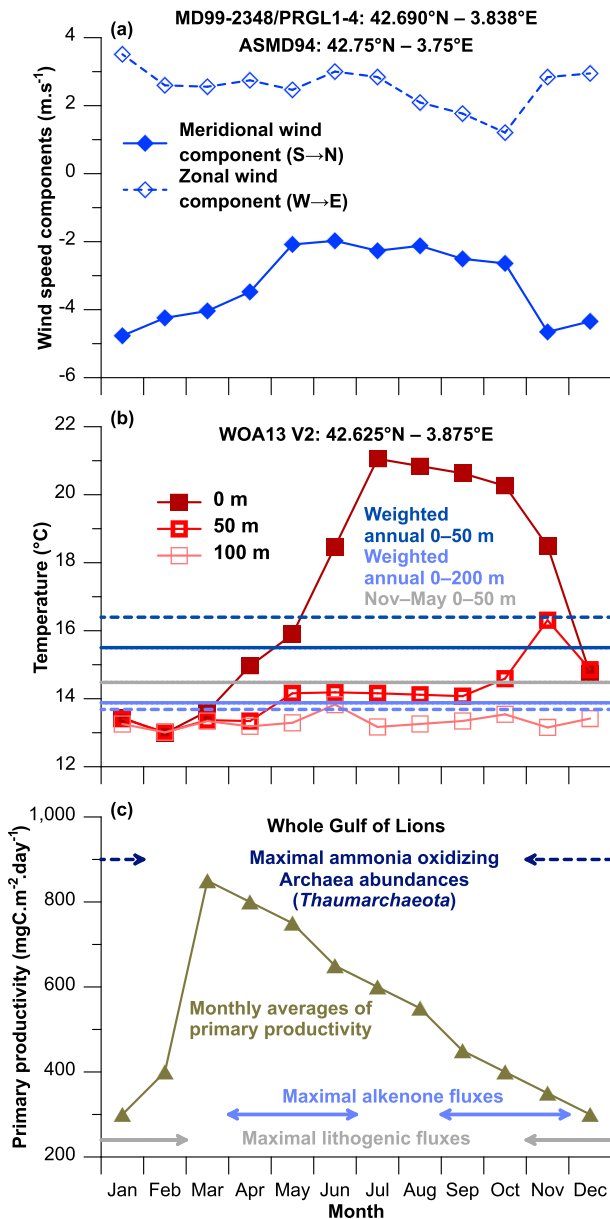


Figure 2. Monthly climatology of wind speed components, sea temperature, and primary productivity estimates at the position of core MD99-2348 and borehole PRGL1-4. The data are from systematically specified positions close to the study site. (a) Zonal and meridional wind speed components (da Silva et al., 1994). Positive values correspond to westerly and southerly winds. (b) Sea temperature at 0-, 50-, and 100-m water depths (Locarnini et al., 2013). The dark blue solid and dashed lines are depth-weighted annual sea temperatures at 0- to 50-m weighted by primary productivity and alkenone fluxes, respectively. The light blue solid and dashed lines are depth-weighted sea temperatures at 0- to 200-m weighted by primary productivity and lithogenic fluxes, respectively. The gray line is the average of monthly depth-weighted annual sea temperatures at 0- to 50-m over the November–May period. (c) Primary productivity estimates (Bosc et al., 2004). The periods of maximal lithogenic particle (gray arrows, Monaco et al., 1990) and alkenone fluxes (light blue double arrows, Sicre et al., 1999; Ternois et al., 1996, 1997) as well as the period of maximal ammonia oxidizing Archaea (*Thaumarchaeota*) abundances (dark blue arrows, Galand et al., 2010) are also shown.

We dissolved the polar fractions in hexane:isopropanol (98.2:1.8, v:v) prior to GDGT analysis on an Agilent 1260 Infinity high performance liquid chromatograph coupled to an Agilent 6120 single quadrupole mass spectrometer installed at CEREGE. We used the same chromatographic columns and solvents as Hopmans et al. (2016), as well as the same elution program, but with a 24-min re-equilibration time. We selected the same atmospheric-pressure chemical ionization source conditions as Davtian et al. (2018): nebulizer pressure, 40 psi; vaporizer temperature, 325 °C; drying gas (N₂) at 4 L/min and 325 °C; capillary voltage, 5 kV (positive mode); corona, 4 μA; and fragmentor, 170 V and 280 V for the internal standard C₄₆ (Huguet et al., 2006) and natural GDGTs, respectively. GDGTs were analyzed in selected ion monitoring (SIM) mode with a dwell time of 77 ms, and all the samples were processed in duplicate. We then used the Chemstation software to quantify GDGTs by extracting the *m/z* values of 1,022.0, 1,036.0, 1,050.0, 1,292.3, 1,296.3, 1,298.3, 1,300.3, and 1,302.4.

Our identification of OH-GDGT peaks is supported by the systematic detection of three peaks between 68 and 73 min, which Hopmans et al. (2016) identified as OH-GDGTs (supporting information Figure S1). In addition, we detected these three late eluting peaks in the *m/z* 1,300.3, 1,298.3, and 1,296.3 SIM scans (supporting information Figure S1). The late eluting peaks in the *m/z* 1,300.3, 1,298.3, and 1,296.3 SIM scans correspond to abundant in-source fragmentation products of OH-GDGTs with molecular masses of 1,318.3, 1,316.3, and 1,314.3 Da (e.g., de Bar et al., 2019; Liu et al., 2012; Yang et al., 2018). We thus quantified OH-GDGTs using the *m/z* 1,300.3, 1,298.3, and 1,296.3 SIM scans (supporting information Figure S1).

3.3. GDGT-Based Proxies and SST Estimates

We calculated RI-OH values (range between 1 and 2) following Lü et al. (2015), where OH-GDGT-X is the OH-GDGT with X pentacycles:

$$RI-OH = \frac{OH-GDGT-1 + 2 \times OH-GDGT-2}{OH-GDGT-1 + OH-GDGT-2} \quad (1)$$

We calculated TEX₈₆ values (range between 0 and 1) following Schouten et al. (2002), where GDGT-X is the iGDGT with X pentacycles:

$$TEX_{86} = \frac{GDGT-2 + GDGT-3 + \text{Crenarchaeol isomer}}{GDGT-1 + GDGT-2 + GDGT-3 + \text{Crenarchaeol isomer}} \quad (2)$$

We calculated the BIT index (branched and isoprenoid tetraether index, range of values between 0 and 1) proposed by Hopmans et al. (2004) as a tracer of terrigenous inputs, as updated by Davtian et al. (2018) to take into account the newest branched GDGT isomers (De Jonge et al., 2013; Ding et al., 2016):

$$BIT = \frac{Ia + IIa_5 + IIIa_5 + IIa_6 + IIIa_6 + IIa_7 + IIIa_7}{\text{Crenarchaeol} + Ia + IIa_5 + IIIa_5 + IIa_6 + IIIa_6 + IIa_7 + IIIa_7} \quad (3)$$

Roman numerals refer to branched GDGT isomers following the nomenclature adopted by Ding et al. (2016).

We calculated the methane index (MI, range of values between 0 and 1) proposed by Zhang et al. (2011) as a tracer of methanotrophic inputs:

$$MI = \frac{GDGT-1 + GDGT-2 + GDGT-3}{GDGT-1 + GDGT-2 + GDGT-3 + \text{Crenarchaeol} + \text{Crenarchaeol isomer}} \quad (4)$$

We calculated the ring index (RI, range of values between 0 and 4) proposed by Zhang et al. (2016) as a tracer of biases for TEX_{86} , where [X] is the fractional abundance of compound X relative to the summed abundance of GDGT-0, GDGT-1, GDGT-2, GDGT-3, crenarchaeol, and crenarchaeol isomer:

$$RI = 0 \times [GDGT-0] + 1 \times [GDGT-1] + 2 \times [GDGT-2] + 3 \times [GDGT-3] + 4 \times [\text{Crenarchaeol}] + 4 \times [\text{Crenarchaeol isomer}] \quad (5)$$

We compared the RI value of each sample, RI_{sample} , with the result of its quadratic regression on TEX_{86} established by Zhang et al. (2016), RI_{TEX} , by calculating ΔRI values:

$$RI_{\text{TEX}} = -0.77(\pm 0.38) \times TEX_{86} + 3.32(\pm 0.34) \times TEX_{86}^2 + 1.59(\pm 0.10), \quad (6)$$

$$\Delta RI = RI_{\text{TEX}} - RI_{\text{sample}} \quad (7)$$

We calculated RI-OH-based SSTs using the global calibration by Lü et al. (2015):

$$SST = \frac{RI-OH-1.11}{0.018} \quad (R^2 = 0.74, n = 107, p < 0.01). \quad (8)$$

We calculated TEX_{86} -based SSTs using the Bayesian, spatially varying calibration by Tierney and Tingley (2014, 2015), BAYSPLINE, with a prior standard deviation (SD) set to 6 °C.

We selected a modern marine sediment from the Bay of Marseille (Mediterranean Sea, 43.26°N, 5.29°E; roughly 60-m water depth, first analyzed by Sanchi et al., 2013) as an in-house standard sediment to check the absence of instrumental drift. Over the course of the present study, the SD of 30 duplicate analyses of a single lipid extract was 0.009 for RI-OH, 0.003 for TEX_{86} , BIT, and MI, and 0.019 for RI. These SD values correspond to ranges of 0.5 and 0.2 °C in RI-OH-SSTs and TEX_{86} -SSTs, respectively. These values are of the same order of magnitude as the average of SD values based on duplicate injections of the entire sample set measured on the two sediment cores: 0.003 for RI-OH, 0.002 for TEX_{86} , 0.001 for BIT and MI, and 0.005 for RI, corresponding to ranges of 0.1–0.2 °C in RI-OH-SSTs and TEX_{86} -SSTs. To be conservative, the SD values obtained on the in-house standard sediment will be used as 1σ uncertainties for the GDGT proxies measured on a single sample.

3.4. BAYSPLINE Calibration for Alkenone-Based SST Estimates

Tierney and Tingley (2018) have suggested that alkenones record November–May SSTs rather than annual SSTs in the Mediterranean Sea. They have also proposed a new Bayesian, Basis-spline calibration, BAYSPLINE, for $U^{K'}_{37}$. We have thus used the BAYSPLINE calibration to calculate November–May SSTs, with a prior SD set to 10 °C. The highest $U^{K'}_{37}$ -SSTs of Cortina et al. (2015) based on the calibration by Müller et al. (1998) were below 23.4 °C during the 160–9 ka BP period. Despite a small shift in $U^{K'}_{37}$ -SSTs by –0.5 °C on average, no change in general trends or amplitudes is observed between the SST records calculated with the two calibrations. The 1σ maximal analytical uncertainty in $U^{K'}_{37}$ -SSTs is roughly 0.5 °C, which is equivalent to 0.015 $U^{K'}_{37}$ units (Martrat et al., 2003).

3.5. Correlation Coefficient and Significance Estimates for Serially Correlated Data

Our quantitative correlation tests between time series follow the same approach as Baddouh et al. (2016). In short, we employed sample interpolation and significance testing with phase-randomized surrogate data (Ebisuzaki, 1997). The creation of phase-randomized surrogates is a nonparametric method that helps to account for serial correlation in time series. In case of different sampling grids, the time series with fewer points in the common interval was used for piecewise linear interpolation. Then, the statistical significance of the resulting correlation coefficients was estimated via 10,000 Monte Carlo simulations using

phase-randomized surrogates (Ebisuzaki, 1997). We did all sample interpolations and quantitative correlation tests using the “surrogateCor” function of the astrochron package for R (Meyers, 2014; R Core Team, 2019).

4. Results and Discussion

4.1. GDGT-Based Paleothermometry in the Gulf of Lions

4.1.1. Thermal Influences on GDGTs

The new records are presented in Figures 3a–3c and supporting information Data Set S1. TEX_{86} values vary between 0.39 and 0.62 (Figure 3a). BIT values vary between 0.07 and 0.57 (Figure 3b). RI-OH values vary between 1.15 and 1.39 (Figure 3c).

Quantitative correlation tests of RI-OH with $U^{K'}_{37}$ (Figure 3d; Cortina et al., 2015) and *Globigerina bulloides* $\delta^{18}\text{O}$ (Figure 3e; Sierro et al., 2009) help to assess the novel organic paleothermometer in the Gulf of Lions. After resampling of RI-OH data ($n = 261$) on the $U^{K'}_{37}$ sample grid ($n = 249$) from 160 to 29 ka BP, a significant correlation is observed between both biomarker-based proxies ($r = 0.65$, $n = 249$, $p < 0.001$, Figures 3c and 3d). Similarly, after resampling of planktic $\delta^{18}\text{O}$ data ($n = 1,027$) on the RI-OH sample grid ($n = 425$) from 160 to 9 ka BP, a significant anticorrelation is observed between both proxies ($r = -0.68$, $n = 425$, $p < 0.001$, Figures 3c and 3e). The significant correlations of RI-OH with $U^{K'}_{37}$ and planktic $\delta^{18}\text{O}$ suggest that all three proxies essentially behave as paleothermometers at the MD99-2348/PRGL1-4 study site.

Visually, TEX_{86} has a different behavior compared to RI-OH, $U^{K'}_{37}$, and planktic $\delta^{18}\text{O}$. After resampling of TEX_{86} data ($n = 261$) on the $U^{K'}_{37}$ sample grid ($n = 249$) from 160 to 29 ka BP, no significant correlation is found between both biomarker-based proxies ($r = -0.09$, $n = 249$, $p = 0.39$, Figures 3a and 3d). Similarly, after resampling of planktic $\delta^{18}\text{O}$ data ($n = 1,027$) on the TEX_{86} sample grid ($n = 425$) from 160 to 9 ka BP, a significant but relatively weak anticorrelation is observed between both proxies ($r = -0.32$, $n = 425$, $p = 0.02$, Figures 3a and 3e). Therefore, TEX_{86} does not behave as well as the other paleothermometers at our study site.

Given the resampling of previously published records from raw MD99-2348/PRGL1-4 sediments, our reported r coefficients likely correspond to worst-case scenarios, because a multiproxy analysis on a single set of sediment samples could give even better correlations between paleothermometric proxies. In addition, alkenones and GDGTs are not analyzed in the same lipid extracts from MD99-2348/PRGL1-4 sediments. For example, using a single set of lipid extracts from the same depths of a sediment core from the Iberian Margin, Darfeuil et al. (2016) have reported an r coefficient of 0.89 ($n = 400$, $p < 0.001$) between TEX_{86} and $U^{K'}_{37}$.

An observation that is not reliant upon the resampling of previously published records is the systematic and coherent response of RI-OH to well-known climatic events. RI-OH has higher values during marine isotope stage (MIS) 5e (mean of 1.29, SD of 0.05, $n = 16$), 5c (mean of 1.27, SD of 0.04, $n = 15$), 5a (mean of 1.26, SD of 0.03, $n = 20$), and 1 (mean of 1.37, SD of 0.01, $n = 8$) than during MIS 6 (mean of 1.22, SD of 0.04, $n = 82$), 5d (mean of 1.23 ± 0.01 , $n = 13$), 5b (mean of 1.22, SD of 0.01, $n = 10$), and 4–2 (mean of 1.20, SD of 0.03, $n = 261$, Figure 3c). The difference between the mean RI-OH value for warm isotope stages (mean of 1.28, SD of 0.05, $n = 59$) and the mean RI-OH value for cold isotope stages (mean of 1.21, SD of 0.03, $n = 366$) is 9 times larger than the mean 1σ analytical uncertainty for RI-OH (0.009). RI-OH also has higher values during Greenland interstadials (mean RI-OH maximum of 1.25, SD of 0.02, $n = 18$) than during Greenland stadials and Heinrich events (mean RI-OH minimum of 1.18, SD of 0.02, $n = 18$, Figure 4c). The difference between the mean RI-OH maximum for Greenland interstadials and the mean RI-OH minimum for Greenland stadials and Heinrich events is 8 times larger than the mean 1σ analytical uncertainty for RI-OH. Such systematic trends are also apparent for $U^{K'}_{37}$ and *Globigerina bulloides* $\delta^{18}\text{O}$ concerning isotope stages (Figures 3d and 3e) and abrupt climatic events (Figures 4d and 4e). By contrast, TEX_{86} does not have systematically higher values during interglacials (MIS 1 and 5e) and Greenland interstadials than during Greenland stadials and Heinrich events (Figures 3a and 4a). Despite the imperfect agreement with $U^{K'}_{37}$ and planktic $\delta^{18}\text{O}$, RI-OH behaves better as a paleothermometer than does TEX_{86} .

4.1.2. Potential Biases for GDGT-Based and Other Paleothermometers

Biases in $U^{K'}_{37}$ and planktic $\delta^{18}\text{O}$ values may partially explain the imperfect agreement with RI-OH. The $\delta^{18}\text{O}$ of planktic foraminifers like *Globigerina bulloides*, while generally consistent with

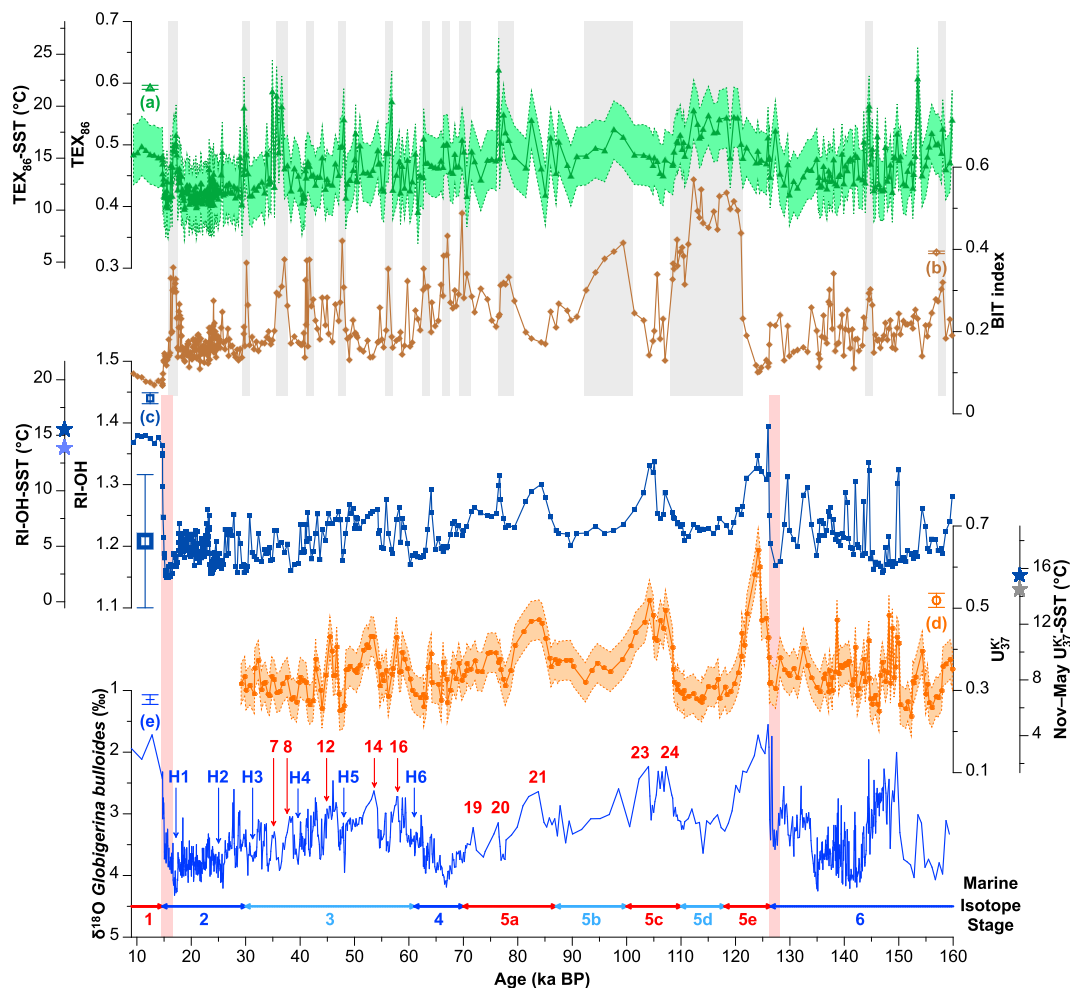


Figure 3. Assessment of archaeal membrane lipids as paleothermometers in core MD99-2348 (25–9 ka BP) and borehole PRGL1-4 (160–23 ka BP). (a) TEX_{86} (TetraEther indeX of tetraethers consisting of 86 carbon atoms; Schouten et al., 2002) with a conversion into sea surface temperatures (SSTs) using the spatially varying BAYSPAR calibration by Tierney and Tingley (2014, 2015). (b) Branched and isoprenoid tetraether (BIT) index as a qualitative indicator of terrigenous inputs (Hopmans et al., 2004), updated by Davtian et al. (2018) to consider the recently identified compounds (De Jonge et al., 2013; Ding et al., 2016). Increased BIT values associated with increased TEX_{86} values are highlighted by light gray shaded areas in Figures 3a and 3b. (c) RI-OH (ring index of hydroxylated tetraethers; Lü et al., 2015) with a conversion into SSTs using the global calibration by Lü et al. (2015): $SST = (RI-OH - 1.11)/0.018$. (d) $U^{K'}_{37}$ (C_{37} ketone unsaturation ratio; Prah & Wakeham, 1987) with a conversion into November–May SSTs using the BAYSPLINE calibration by Tierney and Tingley (2018). Original $U^{K'}_{37}$ data from Cortina et al. (2015). (e) Isotopic composition of the oxygen ($\delta^{18}O$) record of *Globigerina bulloides*: note the reversed axis. Original data from Sierra et al. (2009). The dark blue stars in Figures 3c and 3d indicate the present depth-weighted annual sea temperature at 0- to 50-m weighted by primary productivity. The light blue star in Figure 3c indicates the present depth-weighted annual sea temperature at 0- to 200-m weighted by primary productivity. The gray star in Figure 3d indicates the present average of monthly depth-weighted annual sea temperatures at 0- to 50-m over the November–May period. Small open symbols with colored error bars are 1σ analytical uncertainties. Envelopes in Figures 3a and 3d are 1σ uncertainties in TEX_{86} -SSTs and $U^{K'}_{37}$ -SSTs, which are determined using the 16th and 84th percentiles. The large open symbol with a dark blue error bar in Figure 3c is the 1σ uncertainty in RI-OH-SSTs. Light pink shaded areas in Figures 3c–3e highlight the glacial-interglacial transitions on which the regional comparison of annual SST anomalies in Figure 5 focuses. Red numbers indicate Greenland interstadials. Blue numbers preceded by an “H” indicate Heinrich events. Numbers below the horizontal arrows and double arrows are marine isotope stages according to Railsback et al. (2015).

paleothermometric proxies, is also influenced by the $\delta^{18}O$ of seawater, which is itself influenced by, for instance, fresh water inputs (Sierra et al., 2009). In addition, unrealistically high $U^{K'}_{37}$ -based SSTs from PRGL1-4 sediments—unpublished in the paper by Cortina et al. (2015)—were reported during MIS 2 due to coelutions with alkenones (Rama-Corredor et al., 2018). These coelutions occurred because the MD99-2348/PRGL1-4 study site received substantial terrigenous inputs from the Rhône River during glacial periods (Cortina et al., 2016; Frigola et al., 2012; Pasquier et al., 2017, 2019; Sierra et al., 2009). Therefore, at least some unknown portions of the alkenone-based record by Cortina et al. (2015) could be affected by coelutions, especially during glacial maxima.

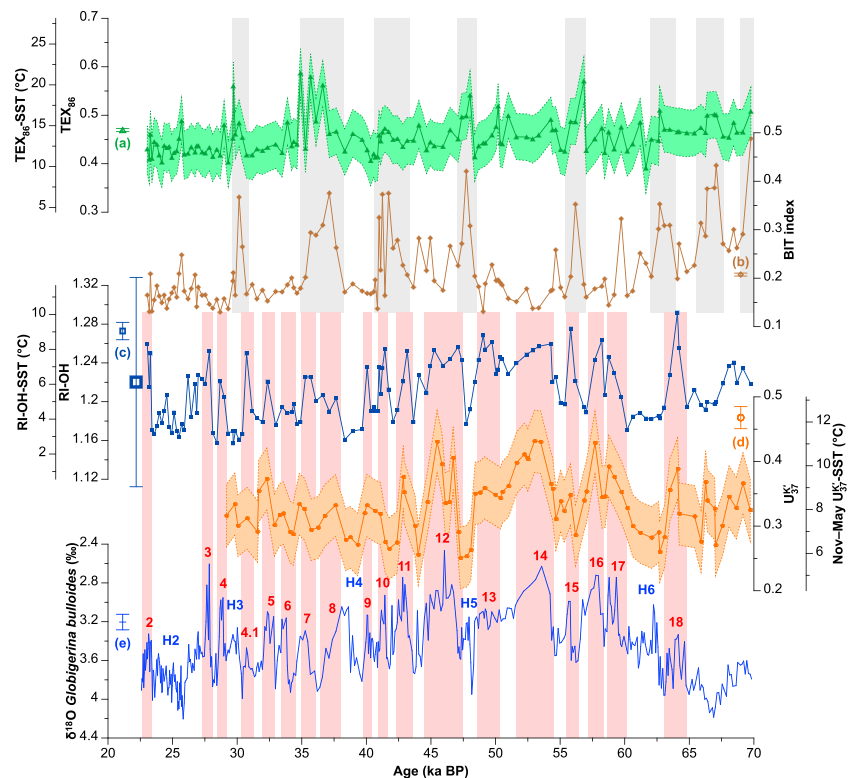


Figure 4. Close-up to 70–20 ka BP of Figure 3. The caption is the same as in Figure 3, except that light pink shaded areas in Figures 4c–4e highlight abrupt warm climatic events as depicted by RI-OH (ring index of hydroxylated tetraethers; Lü et al., 2015).

Given its peculiar context, the MD99-2348/PRGL1-4 study site is prone to substantially biased TEX_{86} values. We thus assessed terrigenous, methanotrophic, and other biases for TEX_{86} using the BIT index (Hopmans et al., 2004), the MI (Zhang et al., 2011), and RI (Zhang et al., 2016), respectively (supporting information Figure S2). While methanotrophic inputs do not seem detectable in most sediment samples (supporting information Figure S2b), the significant correlation between BIT and TEX_{86} ($r = 0.59$, $n = 425$, $p < 0.001$; supporting information Figure S2a, see also Figures 3a, 3b, 4a, and 4b) and $|\Delta RI|$ values mostly above 0.3 (73% of sediment samples; supporting information Figure S2c) in MD99-2348/PRGL1-4 sediments provides a good case against the use of TEX_{86} at our study site.

While RI-OH behaves as a paleothermometer, we have to assess biases, especially terrigenous inputs for this novel proxy as well. Sinninghe Damsté et al. (2012) did not find OH-GDGTs in Group I.1b *Thaumarchaeota*, which is itself a major iGDGT producer in soils. Nevertheless, Kang et al. (2017) have found OH-GDGTs in Korean soils and suggest that terrigenous inputs could lead to a warm bias in RI-OH-SSTs in the eastern Yellow Sea. However, BIT and RI-OH are not correlated in MD99-2348/PRGL1-4 sediments ($r = -0.03$, $n = 425$, $p = 0.91$; Figures 3b and 3c). Therefore, even if OH-GDGTs could be present in soils within the Rhône and Pyreneo-Languedocian drainage basins, the influence of terrigenous inputs on RI-OH values is not as obvious as on TEX_{86} values at our study site.

4.2. Assessment of Temperatures Recorded by OH-GDGTs

4.2.1. Interpretation of Uncertainties in Biomarker-Based Temperature Estimates

TEX_{86} -based SSTs vary between 9.8 and 23.5 °C, with 1σ uncertainties of 2.9 °C (Figure 3a). RI-OH-based SSTs vary between 2.2 and 15.8 °C, with 1σ uncertainties of roughly 6 °C (Figure 3c). $U_{37}^{K'}$ -based November–May SSTs vary between 5.4 and 17.4 °C, with 1σ uncertainties of 1.4 °C (Figure 3d). Given that TEX_{86} provides spurious patterns (section 4.1), we discuss SST estimates from RI-OH and $U_{37}^{K'}$ only.

Uncertainties discussed in section 4.1.1 reflect the analytical precision of measurements of paleothermometric proxies, while uncertainties in biomarker-based SST estimates essentially reflect the internal

scatter of the proxy-SST calibrations. Global calibrations with sediment core tops imply a number of biases at very different geographic locations and water depths. We can cite effects such as differential timings of maximal biomarker production and export, sedimentation rates and conditions at different sites, bioturbation, or differential degradation at various locations (see also section 4.1.2 for other examples of biases). These influences generate biases in proxy values that subsequently contribute to the overall scatter of the proxy calibration. However, the cumulative effect of these biases may not apply to one particular study site. The overall scatter in a core-top proxy calibration should thus be viewed as an upper-bound of the scatter that would be observed by constructing a local calibration through comparison of instrumental SST and proxy variations over an extended period at a specific site.

In addition, it is useful to consider downcore variations of a paleothermometric proxy, before it is converted in terms of SST with the available calibrations. The significance of these proxy variations can be directly assessed by considering the analytical uncertainties. This is because the detection limit of proxy changes is much smaller than uncertainties linked to the SST-proxy calibrations. For example, the 1σ analytical uncertainties for RI-OH (0.009) and $U^{K'}_{37}$ (0.015) are equivalent to 0.5 °C. The observation of significant correlations between paleothermometric proxies, even for rather small amplitudes of changes (roughly 1 °C), and their concomitance with known climatic events (section 4.1.1) is further proof of the temperature sensitivity of these proxies (see Figures 3 and 4). Indeed, the most parsimonious explanation for synchronous changes of RI-OH, $U^{K'}_{37}$, and $\delta^{18}O$ is that seawater temperature changed in the past, even if proxy variations are just above the analytical detection.

4.2.2. Comparison of Two Independent Biomarker-Based SST Records

For the 160–29 ka BP period, differences between RI-OH-SST and $U^{K'}_{37}$ -SST pairs vary between –8.5 and 4.0 °C (mean of –2.0 °C, SD of 1.7 °C, $n = 249$, Figures 3c and 3d). The mean difference between RI-OH-SSTs and $U^{K'}_{37}$ -SSTs is smaller than the conservative uncertainty of a single pair of $U^{K'}_{37}$ -based SST and RI-OH-based SST ($\sigma = \sqrt{[1.4^2 + 6.0^2]} = 6.2$ °C). However, our comparison is based on 249 samples, and the standard error of the mean should be close to $\sigma/\sqrt{n} = 6.2/\sqrt{249} = 0.4$ °C, assuming that all SST pairs provide independent assessments of the same bias. This standard error of the mean difference based on 249 samples is actually close to the analytical errors for the proxies themselves.

Another view of the RI-OH versus $U^{K'}_{37}$ SST bias is given by the fact that among the 249 samples, 223 (90%) exhibit lower RI-OH-SSTs than $U^{K'}_{37}$ -SSTs. Therefore, the mean difference between the two biomarker-based SST records is very systematic, even if it is, admittedly, smaller than the conservative uncertainty of a single RI-OH-SST and $U^{K'}_{37}$ -SST pair.

4.2.3. Consideration of a Regional Calibration Relevant to the Mediterranean Sea

A possibility that should be investigated in a semienclosed basin such as the Mediterranean Sea is the irrelevance of global calibrations to the Gulf of Lions. The semienclosed character of the Mediterranean Sea has motivated several local and regional calibration studies for alkenones and iGDGTs (Kaiser et al., 2014; Kim et al., 2015; Leider et al., 2010; Ternois et al., 1997). In addition, Kim et al. (2015) have confirmed that the spatially varying BAYSPAR calibration by Tierney and Tingley (2014, 2015) captures the regional difference in TEX_{86} sensitivity to SSTs in the Mediterranean Sea. However, since our RI-OH-SST record from the Gulf of Lions is the first published to date, previous studies have not tested the validity of RI-OH in a semienclosed basin as compared to open oceans.

4.2.4. Consideration of Depth of Maximal Biomarker Production

The BAYSPLINE calibration by Tierney and Tingley (2018) presumes that alkenones record SSTs, which is likely in the Gulf of Lions. Alkenone producers need light to thrive, so alkenones are produced in surface waters and within the seasonal thermocline in the northwestern Mediterranean Sea (Cacho, Pelejero, et al., 1999; Sicre et al., 1999; Ternois et al., 1996, 1997). Therefore, the depth-weighted sea temperatures at 0- to 50-m (14.5–16.4 °C, Figure 2b) are the most relevant for $U^{K'}_{37}$ in the Gulf of Lions.

The global calibration by Lü et al. (2015) presumes that OH-GDGTs record SSTs. However, contrary to alkenone producers, archaeal GDGT producers do not need light to thrive, so archaeal GDGTs could record sea subsurface temperatures rather than SSTs (e.g., Huguet et al., 2007; Lee et al., 2008; Xing et al., 2015), even though Zhang and Liu (2018) have recently suggested that TEX_{86} reflects sea temperatures less than 200-m deep. Near the MD99-2348/PRGL1-4 study site, the difference between depth-weighted annual sea temperatures at 0- to 50-m weighted by primary productivity and depth-weighted annual sea temperatures at 0- to

200-m is roughly 1.7 °C (Figure 2b), which is close to the mean difference between $U^{K'}_{37}$ -SSTs and RI-OH-SSTs (2.0 °C, section 4.2.2). This is the basis for our reasonable hypothesis. In the Gulf of Lions, archaeal GDGT producers could thrive in subsurface waters in summer where nutrients are abundant (Cruzado & Velasquez, 1990) and where light could be a limiting factor for phytoplankton growth. Although Lü et al. (2015) did not correlate RI-OH with any subsurface sea temperature, we consider depth-weighted annual sea temperatures at 0- to 200-m in addition to SSTs to test the validity of RI-OH in the Mediterranean Sea.

4.2.5. Consideration of Seasonality of Maximal Biomarker Production

The BAYSPLINE calibration by Tierney and Tingley (2018) presumes that alkenones record November–May SSTs in the Mediterranean Sea, which is likely in the Gulf of Lions. In the northwestern Mediterranean Sea, high alkenone flux periods occur in spring and autumn (Figure 2c; Sicre et al., 1999; Ternois et al., 1996, 1997), and Rigual-Hernández et al. (2013) reported recurring coccolith flux maxima in spring. In addition, Cortina et al. (2015) hypothesized that their $U^{K'}_{37}$ -SSTs correspond to winter-spring SSTs, which is supported by the shift in $U^{K'}_{37}$ -SSTs by only -0.5 °C on average when using the BAYSPLINE calibration. This averaged shift in $U^{K'}_{37}$ -SSTs is half the difference between the depth-weighted annual sea temperature at 0- to 50-m weighted by primary productivity (15.5 °C, Figure 2b) and the average of monthly depth-weighted annual sea temperatures at 0- to 50-m over the November–May period (14.5 °C, Figure 2b). This suggests that the depth-weighted annual sea temperature at 0- to 50-m weighted by primary productivity is more relevant to $U^{K'}_{37}$ than is the depth-weighted annual sea temperature at 0- to 50-m weighted by alkenone fluxes (16.4 °C, Figure 2b) in the Gulf of Lions.

The global calibration by Lü et al. (2015) presumes that OH-GDGTs record annual SSTs, which may not be true in the Gulf of Lions. Galand et al. (2010) observed maximal *Thaumarchaeota* abundances in the coastal northwestern Mediterranean Sea (Blanes Bay Microbial Observatory) in winter (Figure 2c). The observed biomarker production maxima in winter-spring are related to increased nutrient content of Mediterranean surface waters as a result of regional circulation and wind-driven deep convection (D'Ortenzio et al., 2014). Assuming that *Thaumarchaeota* also thrives in summer but within and below the seasonal thermocline where nutrients are more abundant (Cruzado & Velasquez, 1990), OH-GDGTs should record sea temperatures that are 0.6 to 1.8 °C colder than those recorded by alkenones. Therefore, depending on the seasonality and depth of maximal biomarker production, the seasonal bias explains between one third and the near totality of the systematic difference between $U^{K'}_{37}$ -SSTs and RI-OH-SSTs.

4.2.6. Provisional Conclusions and Caveats to Address Concerning Temperatures Recorded by OH-GDGTs

Based on the discussion in sections 4.2.4 and 4.2.5, we suggest that RI-OH records winter SSTs and/or subsurface temperatures rather than annual SSTs. However, archaeal GDGT producers in subsurface waters are not necessarily identical to those in surface waters, which could bias SST estimates (e.g., Kim et al., 2015, 2016; Zhu et al., 2016). In addition, our provisional conclusions assume a similar seasonality and depth of maximal OH-GDGT and alkenone production during glacial and interglacial periods, as well as a water column temperature profile with a constant structure through time. In all cases, both the seasonality and depth of maximal OH-GDGT production must be considered in a future regional calibration of RI-OH in the Mediterranean Sea.

4.3. Regional Comparison of Interglacial-Glacial SST Anomalies

4.3.1. Observed SST Anomalies and Proxy-Proxy Comparisons

Our multiproxy comparison of annual SST anomalies for the latest two glacial-interglacial transitions focuses on the Iberian Margin, the Gulf of Cadiz, and the western Mediterranean Sea, including the Siculo-Tunisian Strait (Figure 5 and supporting information Data Set S2). The use of microfossil assemblages allows to consider the different seasons for SST anomalies (Table 1). We have considered only those published records that include both the Holocene (after 11.7 ka BP) and/or Eemian interglacial (~129–112 ka BP) and preceding glacial maximum, which is the Last Glacial Maximum (LGM, ~21 ka BP) and the end of MIS 6 (~140 ka BP), respectively. We have found fewer records containing the MIS 6-Eemian transition (Figure 5b) than records containing the LGM-Holocene transition (Figure 5a), essentially due to a lack of availability of published long records. We define SST anomalies as the difference between the interglacial optimum and the preceding glacial maximum, rounded to the closest unit – SST anomaly = SST interglacial optimum – SST glacial maximum.

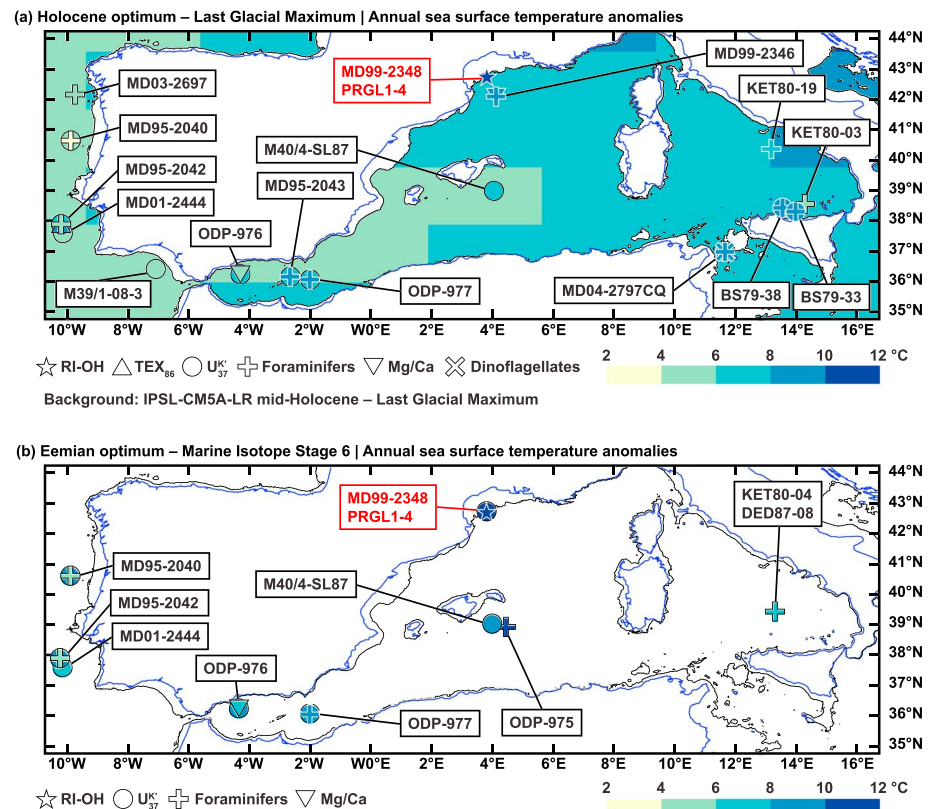


Figure 5. Multiproxy comparison of annual sea surface temperature (SST) anomalies for the latest two glacial-interglacial transitions in the Iberian Margin, the Gulf of Cadiz, and the western Mediterranean Sea, including the Siculo-Tunisian Strait. The anomalies are defined as the difference between the interglacial optimum and the preceding glacial maximum, rounded to the closest unit – SST anomaly = SST interglacial optimum – SST glacial maximum. (a) Holocene optimum-Last Glacial Maximum anomalies. The ocean background is colored according to the mid-Holocene-Last Glacial Maximum annual SST anomalies based on the IPSL-CM5A-LR model (Dufresne et al., 2013; see Figure 6a for a motivation for the model choice). Observed and modeled anomalies follow the same color coding. (b) Eemian optimum-marine isotope stage 6 anomalies. Anomalies in Figures 5a and 5b follow the same color coding. RI-OH (ring index of hydroxylated tetraethers; Lü et al., 2015), TEX_{86} (TetraEther index of tetraethers consisting of 86 carbon atoms; Schouten et al., 2002), and $U^{K'}_{37}$ (C_{37} ketone unsaturation ratio; Prahl & Wakeham, 1987) are three independent organic paleothermometers. The spatially varying BAYSPAR calibration (Tierney & Tingley, 2014, 2015) gives the same TEX_{86} -based anomaly as the regional paleocalibration by Darfeuille et al. (2016) at the MD95-2042 site. With the exception of the MD04-2797CQ site, little or no change in $U^{K'}_{37}$ -based anomalies is expected when using the BAYSPLINE calibration by Tierney and Tingley (2018) rather than the calibrations used by the authors of selected $U^{K'}_{37}$ -based SST records. In the Mediterranean Sea, $U^{K'}_{37}$ reflects November–May rather than annual SSTs (Tierney & Tingley, 2018). The Mg/Ca ratio was measured on *Globigerina bulloides* at the sites selected for this regional comparison (Boussetta et al., 2012; Jiménez-Amat & Zahn, 2015). Microfossil-based anomalies do not all correspond to annual SST (see Table 1 and supporting information Data Set S2 for further information). All the observed SST anomalies are directly based on the following publications: MD99-2348 and PRGL1-4 (Cortina et al., 2015; this study), MD99-2346 (Boussetta et al., 2012; Melki et al., 2009), MD03-2697 (Sánchez Goñi et al., 2008), MD95-2040 (de Abreu et al., 2003; Pailler & Bard, 2002), MD95-2042 (Cayre et al., 1999; Darfeuille et al., 2016; Pailler & Bard, 2002), MD01-2444 (Martrat et al., 2007), M39/1-08-3 (M39-008; Cacho et al., 2001), ODP-976 (Jiménez-Amat & Zahn, 2015; Martrat et al., 2014), ODP-977 (Martrat et al., 2004; Pérez-Folgado et al., 2004), MD95-2043 (Cacho, Grimalt, et al., 1999; Pérez-Folgado et al., 2003), M40/4-SL87 (Emeis et al., 2003), ODP-975 (Kandiano et al., 2014), BS79-33 (Cacho et al., 2001; Sbaifi et al., 2001), BS79-38 (Cacho et al., 2001; Sbaifi et al., 2001), KET80-03 (Kallel et al., 1997), KET80-19 (Kallel et al., 1997), KET80-04 and DED87-08 (Kallel et al., 2000), and MD04-2797CQ (Essallami et al., 2007; Rouis-Zargouni et al., 2010; Sicre et al., 2013). The MD99-2348/PRGL1-4 study site is highlighted in red. The present (blue lines) and glacial maxima (black lines, assuming lowstands with a relative sea level of -120 m; Zickel et al., 2016) coastlines are also shown.

Observed annual SST anomalies vary between 3 and 10 °C for the LGM-Holocene transition (Figures 5a and 6a) and between 4 and 11 °C for the MIS 6-Eemian transition (Figures 5b and 6b). For the published records that contain the latest two glacial-interglacial transitions, annual SST anomalies are often larger for the MIS

Table 1
Annual and Seasonal Microfossil-Based Sea Surface Temperature (SST) Anomalies

Core(s)	Proxy	Transition ^a	Annual	Winter ^b	Spring ^b	Summer ^b	Autumn ^b	Reference(s)
MD99-2346	Foraminifers	MIS 2 → 1	N/A	N/A	9	N/A	N/A	Boussetta et al. (2012), Melki et al. (2009)
MD03-2697	Foraminifers	MIS 2 → 1	N/A	4	N/A	4	N/A	Sánchez Goñi et al. (2008)
MD95-2040	Foraminifers	MIS 2 → 1	N/A	N/A	N/A	3	N/A	de Abreu et al. (2003)
		MIS 6 → 5e	N/A	N/A	N/A	4	N/A	
MD95-2042	Foraminifers	MIS 2 → 1	N/A	4	N/A	4	N/A	Cayre et al. (1999)
		MIS 6 → 5e	N/A	5	N/A	4	N/A	
ODP-977	Foraminifers	MIS 2 → 1	8	7	8	10	8	Pérez-Folgado et al. (2004)
		MIS 6 → 5e	8	7	8	11	9	
MD95-2043	Foraminifers	MIS 2 → 1	8	7	8	11	9	Pérez-Folgado et al. (2003)
ODP-975	Foraminifers	MIS 6 → 5e	N/A	10	N/A	12	N/A	Kandiano et al. (2014)
BS79-33	Foraminifers	MIS 2 → 1	9	7	8	13	10	Sbaffi et al. (2001)
BS79-38	Foraminifers	MIS 2 → 1	9	6	7	12	10	Sbaffi et al. (2001)
KET80-03	Foraminifers	MIS 2 → 1	N/A	3	3	9	N/A	Kallel et al. (1997)
KET80-19	Foraminifers	MIS 2 → 1	N/A	4	5	9	N/A	Kallel et al. (1997)
KET80-04	Foraminifers	MIS 6 → 5e	N/A	N/A	7	N/A	N/A	Kallel et al. (2000)
DED87-08								
MD04-2797CQ	Foraminifers	MIS 2 → 1	N/A	N/A	8	N/A	10	Essallami et al. (2007)
	Dinoflagellates	MIS 2 → 1	N/A	N/A	9	N/A	N/A	Rouis-Zargouni et al. (2010)

Note. The regional comparison of microfossil-based SST anomalies focuses on the latest two glacial-interglacial transitions in the Iberian Margin and the western Mediterranean Sea, including the Siculo-Tunisian Strait. The anomalies are defined as the difference between the interglacial optimum and the preceding glacial maximum, rounded to the closest unit – SST anomaly = SST interglacial optimum – SST glacial maximum. N/A = not applicable.

^aTransitions MIS 2 → 1 and MIS 6 → 5e refer to Holocene optimum – Last Glacial Maximum anomalies and Eemian optimum – marine isotope stage 6 anomalies, respectively. ^bIn general, winter corresponds to February, spring corresponds to April–May, summer corresponds to August, and autumn corresponds to October–November.

6-Eemian transition (Figure 5b) than for the LGM-Holocene transition (Figure 5a). The MD99-2348/PRGL1-4 study site has one of the largest annual SST anomalies for the latest two glacial-interglacial transitions (10 °C, Figure 5). For the LGM-Holocene transition, annual SST anomalies are smaller in the Iberian Margin and the Gulf of Cadiz (5 °C on average, Figure 6a) than in the western Mediterranean Sea (averages per basin between 6 and 9 °C, Figure 6a), with the largest anomalies in the Gulf of Lions and the Siculo-Tunisian Strait (Figures 5a and 6a). For the MIS 6-Eemian transition, annual SST anomalies are also smaller in the Iberian Margin (6.4 °C on average, Figure 6b) than in the western Mediterranean Sea (averages per basin between 7 and 10 °C, Figure 6b), with the largest anomalies in the Gulf of Lions and the Balearic Sea (Figures 5b and 6b). The Gulf of Lions has annual SST anomalies between 8 and 10 °C for the latest two glacial-interglacial transitions, which is within the high end of interglacial-glacial anomalies from previously published records in the western Mediterranean Sea (Figures 5, 6a, and 6b).

Our reported regional differences in interglacial-glacial annual SST anomalies are consistent with previous studies. MARGO Project Members (2009) reported smaller modern-LGM annual SST anomalies in the Iberian Margin than in the western Mediterranean Sea. In addition, Hayes et al. (2005) reported regional differences in modern-LGM annual SST anomalies within the western Mediterranean Sea, with the largest anomalies in the Gulf of Lions. The Mediterranean Sea is a semienclosed basin under the influence of northwesterly winds (Pinardi & Masetti, 2000), so this basin is particularly sensitive to the polar amplification of temperature changes (Braconnot et al., 2012; Izumi et al., 2013; Masson-Delmotte et al., 2006a, 2006b). Furthermore, the Gulf of Lions is directly under the influence of offshore winds (Figures 1 and 2a), which makes this basin sensitive to the land-ocean contrast of temperature changes (Braconnot et al., 2012; Harrison et al., 2016; Izumi et al., 2013; Schmidt, Annan, et al., 2014). The semienclosed character of the Mediterranean Sea and the influence of northwesterly winds likely explain the relatively large interglacial-glacial annual SST anomalies in the Gulf of Lions, which RI-OH successfully records (Figure 3c).

RI-OH and $U^{K'}_{37}$ give the same annual SST anomaly for the MIS 6-Eemian transition at the MD99-2348/PRGL1-4 study site (10 °C, Figure 5b). At the selected sites from the Siculo-Tunisian Strait and the Tyrrhenian Sea, the available paleothermometers all give the same annual SST anomaly per site for the LGM-Holocene transition (Figure 5a). At the other selected sites, the available paleothermometers disagree by 1 to 4 °C on annual SST anomalies for the latest two glacial-interglacial transitions (Figure 5). For the

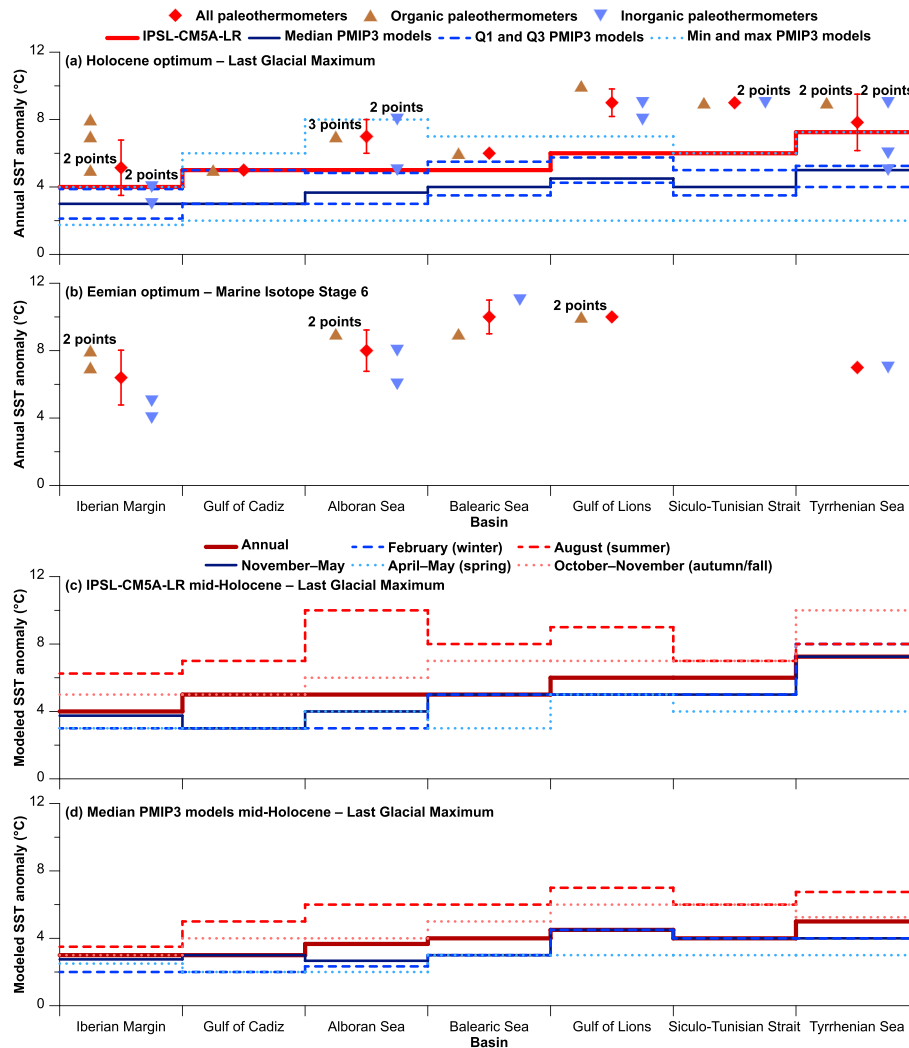


Figure 6. Averaged sea surface temperature (SST) anomalies for the latest two glacial-interglacial transitions per basin. The anomalies are defined as the difference between the interglacial optimum and the preceding glacial maximum, rounded to the closest unit – SST anomaly = SST interglacial optimum – SST glacial maximum. (a) Holocene optimum-Last Glacial Maximum anomalies. Thick solid lines indicate averaged mid-Holocene-Last Glacial Maximum annual SST anomalies per basin based on the IPSL-CM5A-LR model (Dufresne et al., 2013) and on the ensemble median of all Paleoclimate Modeling Intercomparison Project Phase 3 (PMIP3) models with Last Glacial Maximum and mid-Holocene runs-IPSL-CM5A-LR (Dufresne et al., 2013), FGOALS-g2 (Li et al., 2013), CNRM-CM5 (Volodire et al., 2013), MIROC-ESM (Watanabe et al., 2011), MRI-CGCM3 (Yukimoto et al., 2012), CCSM4 (Gent et al., 2011), MPI-ESM-P (Giorgetta et al., 2013), and GISS-E2-R (Schmidt, Kelley, et al., 2014). The ensemble extrema and quartiles of PMIP3 models are also shown for completeness. (b) Eemian optimum-marine isotope stage 6 anomalies. (c) Mid-Holocene-Last Glacial Maximum anomalies based on the IPSL-CM5A-LR model (Dufresne et al., 2013). (d) Mid-Holocene-Last Glacial Maximum anomalies based on the ensemble median of PMIP3 models. Red error bars on red diamonds in Figures 6a and 6b are 1σ standard deviations of the mean annual SST anomalies per basin. Individual annual SST anomalies are also shown in Figures 6a and 6b, with a distinction between organic (brown triangles) and inorganic (blue inverted triangles) paleothermometers.

LGM-Holocene transition, observed disagreements are of 1 to 2 °C, except at the MD95-2042 site where organic paleothermometers and foraminifers give annual SST anomalies that differ by 3–4 °C (Figure 5a). For the MIS 6-Eemian transition, observed disagreements are of 3 to 4 °C, except at the ODP-977 site where alkenones and foraminifers give annual SST anomalies that differ by only 1 °C (Figure 5b). In the Iberian Margin, organic paleothermometers systematically give larger annual SST anomalies than do foraminifers (Figures 5, 6a, and 6b). Our reported disagreements are essentially due to the independence of the paleothermometers considered in the regional comparison (Bard, 2001; Kucera et al., 2005). Despite the differences in annual SST anomalies between independent paleothermometers, the regional difference in annual SST anomalies between the Iberian Margin and the western Mediterranean Sea is visible, regardless of the inorganic or organic character of the available paleothermometers (Figures 5, 6a, and 6b).

Our interglacial-glacial SST anomalies are larger in summer-autumn (between 8 and 13 °C) than in winter-spring (between 3 and 10 °C) in the western Mediterranean Sea (Table 1). Similarly, Hayes et al. (2005) reported larger SST anomalies in summer than in winter in the western Mediterranean Sea. Many microfossil-based SST anomalies reported in Figure 5 are not based on an average of all four seasons (Table 1 and supporting information Data Set S2). In addition, $U_{37}^{K'}$ reflects November–May rather than annual SSTs in the Mediterranean Sea (Tierney & Tingley, 2018). Despite these caveats, the regional difference in annual SST anomalies between the Iberian Margin and the western Mediterranean Sea is still visible. The consideration of seasonality also confirms that our RI-OH-based SST anomalies of 10 °C from the Gulf of Lions belong to the high end of interglacial-glacial anomalies from previously published records in the western Mediterranean Sea.

4.3.2. Modeled SST Anomalies and Data-Model Comparisons

In addition to the multiproxy comparison, we took advantage of Paleoclimate Modeling Intercomparison Project Phase 3 (PMIP3) models, which provide complementary information concerning SST anomalies for the LGM-Holocene transition (Braconnot et al., 2011, 2012). To that end, we define modeled SST anomalies as the difference between the mid-Holocene (6 ka BP) and the LGM (21 ka BP), rounded to the closest unit – modeled SST anomaly = modeled SST mid-Holocene – modeled SST LGM. Furthermore, we define data-model disagreements as the difference between observed and modeled SST anomalies, both rounded to the closest unit – data-model disagreement = observed SST anomaly – modeled SST anomaly, with observed SST anomaly = observed SST mid-Holocene – observed SST LGM. We used all PMIP3 models with available LGM and mid-Holocene runs (Figure 6a and supporting information Data Set S3). The following analysis focuses on the ensemble median of PMIP3 models, with special attention to the IPSL-CM5A-LR model (Dufresne et al., 2013) for its best correlation and smallest residuals with the dataset of MARGO Project Members (2009) as stated by Hossain et al. (2018), hence the model choice in Figure 5a.

The IPSL-CM5A-LR model and the ensemble median of PMIP3 models suggest a west-east gradient in annual SST anomalies (Figure 6a). This west-east gradient in SST anomalies, while not always monotonic, still holds when considering seasonality for the IPSL-CM5A-LR model (Figure 6c) and the ensemble median of PMIP3 models (Figure 6d). Furthermore, the IPSL-CM5A-LR model and the ensemble median of PMIP3 models suggest larger SST anomalies in summer-autumn than in winter-spring in the western Mediterranean Sea (Figures 6c and 6d). Therefore, PMIP3 models generally reproduce the regional differences and seasonal contrasts in SST suggested by several independent paleothermometers, including RI-OH.

RI-OH-based SST anomalies agree better with summer-autumn (data-model disagreements of 1–4 °C) than with winter-spring modeled SST anomalies (data-model disagreements of 5–7 °C, Figures 6c and 6d), which does not mean that RI-OH is biased toward summer-autumn in the Gulf of Lions (see section 4.2.5). When comparing $U_{37}^{K'}$ -based SST anomalies with November–May modeled SST anomalies in the Mediterranean Sea following Tierney and Tingley (2018), data-model disagreements increased by 0 to 2 °C compared to annual modeled SST anomalies (Figures 6c and 6d). Data-model disagreements are likely due to misinterpreted and/or biased observed SST anomalies as well as to model deficiencies, so the appropriate season for data-model comparisons cannot be selected for RI-OH until this paleothermometer is further studied in the Mediterranean Sea (see section 4.2.6).

Overall, PMIP3 models suggest the same general trends in SST anomalies as several independent paleothermometers, including RI-OH despite the data-model disagreements in the western Mediterranean Sea. The Iberian Margin has smaller SST anomalies than the western Mediterranean Sea, including the Gulf of Lions. In addition, SST anomalies are smaller in winter-spring than in summer-autumn. Consideration of the season best reflected by independent paleothermometers rather than annual SSTs does not always result in smaller data-model residuals, so we do not recommend assessing seasonal biases using best fit data-model comparisons.

5. Conclusions and Perspectives

The new temperature record we have generated using the novel RI-OH proxy in the Gulf of Lions (western Mediterranean Sea) is generally consistent with other paleothermometric proxies. For the first time, we show that RI-OH responds systematically and coherently to glacial-interglacial transitions as well as to abrupt climatic events such as Greenland interstadials and Heinrich events in the Mediterranean Sea.

However, RI-OH-based temperatures differ by $-2.0\text{ }^{\circ}\text{C}$ on average from November–May $\text{U}^{\text{K}'}_{37}$ -based temperatures. This mean difference is smaller than the conservative uncertainty of a single pair of $\text{U}^{\text{K}'}_{37}$ -based SST and RI-OH-based SST, but our comparison is based on 249 samples leading to a standard error of the mean around $0.4\text{ }^{\circ}\text{C}$. The difference is thus systematic and statistically significant. We suggest that RI-OH and $\text{U}^{\text{K}'}_{37}$ record different temperatures, for instance, winter and/or subsurface temperatures for RI-OH. Full understanding awaits, partly because no regional calibration relevant to the Mediterranean Sea is available as yet for RI-OH.

Both biomarker-based temperature records from the Gulf of Lions give an interglacial-glacial anomaly of $10\text{ }^{\circ}\text{C}$, which is within the high end of annual and seasonal interglacial-glacial anomalies from previously published records in the western Mediterranean Sea (from 3 to $13\text{ }^{\circ}\text{C}$). Furthermore, our RI-OH record confirms the regional differences and seasonal contrasts in interglacial-glacial anomalies produced by PMIP3 models.

Acknowledgments

Work at CEREGE is supported by the Collège de France and BNP-Paribas Foundation (project CPATEMP). N. D. expresses her thanks to the Ecole Normale Supérieure de Lyon and Collège de France for providing PhD salary support. We thank Nicolas Thouveny for providing the U-Channels and sediment cubes that he took for paleomagnetism measurements before this study. We also thank Francisco Sierra for providing the $\delta^{18}\text{O}$ values of *Globigerina bulloides* from core MD99-2348 and borehole PRGL1-4. We are grateful to Jessica Tierney, Yige Zhang, and an anonymous reviewer for their suggestions for improvement of this paper. The new data from core MD99-2348 and borehole PRGL1-4 are provided in supporting information Data Set S1, as well as in the public repository PANGAEA*. The observed interglacial-glacial sea surface temperature anomalies are provided in Table 1 and supporting information Data Set S2. The modeled interglacial-glacial sea surface temperature anomalies have been accessed using the Institut Pierre Simon Laplace Earth System Grid Federation node (<https://esgf-node.ipsl.upmc.fr/projects/esgf-ipsl/>); project “PMIP3”; experiments “midHolocene” and “Igm”; time frequency “monClim”; variable “ts”; and variable long name “Surface Temperature”) and are provided in supporting information Data Set S3. This work was supported by the European Commission Project PROMESS1 (contract EVR1-CT-2002-40024) and the IMAGES program that funded the drilling and coring of the Gulf of Lions. We acknowledge the World Climate Research Programme’s Working Group on Coupled Modeling, which is responsible for CMIP, and we thank the modeling groups (listed in this paper) for producing and making available their model output. For CMIP the U.S. Department of Energy’s Program for Climate Model Diagnosis and Intercomparison provides coordinating support and led development of software infrastructure in partnership with the Global Organization for Earth System Science Portals.

References

- Andersen, K. K., Svensson, A., Johnsen, S. J., Rasmussen, S. O., Bigler, M., Röthlisberger, R., et al. (2006). The Greenland ice core chronology 2005, 15–42 ka. Part 1: Constructing the time scale. *Quaternary Science Reviews*, *25*(23–24), 3246–3257. <https://doi.org/10.1016/j.quascirev.2006.08.002>
- Baddouh, M., Meyers, S. R., Carroll, A. R., Beard, B. L., & Johnson, C. M. (2016). Lacustrine $^{87}\text{Sr}/^{86}\text{Sr}$ as a tracer to reconstruct Milankovitch forcing of the Eocene hydrologic cycle. *Earth and Planetary Science Letters*, *448*, 62–68. <https://doi.org/10.1016/j.epsl.2016.05.007>
- Bard, E. (2001). Comparison of alkenone estimates with other paleotemperature proxies. *Geochemistry, Geophysics, Geosystems*, *2*(1), 1002. <https://doi.org/10.1029/2000GC000050>
- Bosc, E., Bricaud, A., & Antoine, D. (2004). Seasonal and interannual variability in algal biomass and primary production in the Mediterranean Sea, as derived from 4 years of SeaWiFS observations. *Global Biogeochemical Cycles*, *18*, GB1005. <https://doi.org/10.1029/2003GB002034>
- Boussetta, S., Kallel, N., Bassinot, F., Labeyrie, L., Duplessy, J.-C., Caillon, N., et al. (2012). Mg/Ca-paleothermometry in the western Mediterranean Sea on planktonic foraminifer species *Globigerina bulloides*: constraints and implications. *Comptes Rendus Geoscience*, *344*(5), 267–276. <https://doi.org/10.1016/j.crte.2012.02.001>
- Braconnot, P., Harrison, S. P., Kageyama, M., Bartlein, P. J., Masson-Delmotte, V., Abe-Ouchi, A., et al. (2012). Evaluation of climate models using palaeoclimatic data. *Nature Climate Change*, *2*(6), 417–424. <https://doi.org/10.1038/nclimate1456>
- Braconnot, P., Harrison, S. P., Otto-Bliesner, B., Abe-Ouchi, A., Jungclauss, J., & Peterschmitt, J.-Y. (2011). The Paleoclimate Modeling Intercomparison Project contribution to CMIP5. *CLIVAR Exchanges*, *56*(16), 15–19.
- Cacho, I., Grimalt, J. O., Canals, M., Sbaiffi, L., Shackleton, N. J., Schönfeld, J., & Zahn, R. (2001). Variability of the western Mediterranean Sea surface temperature during the last 25,000 years and its connection with the Northern Hemisphere climatic changes. *Paleoceanography*, *16*(1), 40–52. <https://doi.org/10.1029/2000PA000502>
- Cacho, I., Grimalt, J. O., Pelejero, C., Canals, M., Sierro, F. J., Flores, J. A., & Shackleton, N. J. (1999). Dansgaard-Oeschger and Heinrich event imprints in Alboran Sea paleotemperatures. *Paleoceanography*, *14*(6), 698–705. <https://doi.org/10.1029/1999PA900044>
- Cacho, I., Pelejero, C., Grimalt, J. O., Calafat, A., & Canals, M. (1999). C_{37} alkenone measurements of sea surface temperature in the Gulf of Lions (NW Mediterranean). *Organic Geochemistry*, *30*(7), 557–566. [https://doi.org/10.1016/S0146-6380\(99\)00038-8](https://doi.org/10.1016/S0146-6380(99)00038-8)
- Cayre, O., Lancelot, Y., Vincent, E., & Hall, M. A. (1999). Paleoclimatographic reconstructions from planktonic foraminifera off the Iberian Margin: Temperature, salinity, and Heinrich events. *Paleoceanography*, *14*(3), 384–396. <https://doi.org/10.1029/1998PA900027>
- Cortina, A., Grimalt, J. O., Rigual-Hernández, A., Ballegeer, A.-M., Martrat, B., Sierro, F. J., & Flores, J. A. (2016). The impact of ice-sheet dynamics in western Mediterranean environmental conditions during Terminations. An approach based on terrestrial long chain *n*-alkanes deposited in the upper slope of the Gulf of Lions. *Chemical Geology*, *430*, 21–33. <https://doi.org/10.1016/j.chemgeo.2016.03.015>
- Cortina, A., Sierro, F. J., Flores, J. A., Martrat, B., & Grimalt, J. O. (2015). The response of SST to insolation and ice sheet variability from MIS 3 to MIS 11 in the northwestern Mediterranean Sea (Gulf of Lions). *Geophysical Research Letters*, *42*, 10,366–10,374. <https://doi.org/10.1002/2015GL065539>
- Cruzado, A., & Velasquez, Z. R. (1990). Nutrients and phytoplankton in the Gulf of Lions, northwestern Mediterranean. *Continental Shelf Research*, *10*(9–11), 931–942. [https://doi.org/10.1016/0278-4343\(90\)90068-W](https://doi.org/10.1016/0278-4343(90)90068-W)
- Darfeuil, S., Ménot, G., Giraud, X., Rostek, F., Tachikawa, K., Garcia, M., & Bard, E. (2016). Sea surface temperature reconstructions over the last 70 kyr off Portugal: Biomarker data and regional modeling. *Paleoceanography*, *31*, 40–65. <https://doi.org/10.1002/2015PA002831>
- Davtian, N., Bard, E., Ménot, G., & Fagault, Y. (2018). The importance of mass accuracy in selected ion monitoring analysis of branched and isoprenoid tetraethers. *Organic Geochemistry*, *118*, 58–62. <https://doi.org/10.1016/j.orggeochem.2018.01.007>
- da Silva, A., Young, A. C., & Levitus, S. (1994). *Atlas of surface marine data 1994, Vol. 1: Algorithms and procedures*, NOAA Atlas NESDIS (Vol. 6). Washington, DC: US Department of Commerce. Retrieved from <https://iridl.ldeo.columbia.edu/SOURCES/.DASILVA/.SMD94/.halfbyhalf/.climatology/>
- de Abreu, L., Shackleton, N. J., Schönfeld, J., Hall, M. A., & Chapman, M. (2003). Millennial-scale oceanic climate variability off the Western Iberian margin during the last two glacial periods. *Marine Geology*, *196*(1–2), 1–20. [https://doi.org/10.1016/S0025-3227\(03\)00046-X](https://doi.org/10.1016/S0025-3227(03)00046-X)
- de Bar, M. W., Rampen, S. W., Hopmans, E. C., Sinnighe Damsté, J. S., & Schouten, S. (2019). Constraining the applicability of organic paleotemperature proxies for the last 90 Myrs. *Organic Geochemistry*, *128*, 122–136. <https://doi.org/10.1016/j.orggeochem.2018.12.005>
- De Jonge, C., Hopmans, E. C., Stadnitskaia, A., Rijpstra, W. I. C., Hofland, R., Tegelaar, E., & Sinnighe Damsté, J. S. (2013). Identification of novel penta- and hexamethylated branched glycerol dialkyl glycerol tetraethers in peat using HPLC-MS², GC-MS and GC-SMB-MS. *Organic Geochemistry*, *54*, 78–82. <https://doi.org/10.1016/j.orggeochem.2012.10.004>

- Ding, S., Schwab, V. F., Ueberschaar, N., Roth, V. N., Lange, M., Xu, Y., et al. (2016). Identification of novel 7-methyl and cyclopentanyl branched glycerol dialkyl glycerol tetraethers in lake sediments. *Organic Geochemistry*, *102*, 52–58. <https://doi.org/10.1016/j.orggeochem.2016.09.009>
- D'Ortenzio, F., Lavigne, H., Besson, F., Claustre, H., Coppola, L., Garcia, N., et al. (2014). Observing mixed layer depth, nitrate and chlorophyll concentrations in the northwestern Mediterranean: A combined satellite and NO₃ profiling floats experiment. *Geophysical Research Letters*, *41*, 6443–6451. <https://doi.org/10.1002/2014GL061020>
- Dufresne, J.-L., Foujols, M.-A., Denvil, S., Caubel, A., Marti, O., Aumont, O., et al. (2013). Climate change projections using the IPSL-CM5 Earth System Model: From CMIP3 to CMIP5. *Climate Dynamics*, *40*(9–10), 2123–2165. <https://doi.org/10.1007/s00382-012-1636-1>
- Ebisuzaki, W. (1997). A method to estimate the statistical significance of a correlation when the data are serially correlated. *Journal of Climate*, *10*(9), 2147–2153. [https://doi.org/10.1175/1520-0442\(1997\)010<2147:AMTETS>2.0.CO;2](https://doi.org/10.1175/1520-0442(1997)010<2147:AMTETS>2.0.CO;2)
- Elling, F. J., Könneke, M., Lipp, J. S., Becker, K. W., Gagen, E. J., & Hinrichs, K.-U. (2014). Effects of growth phase on the membrane lipid composition of the thaumarchaeon *Nitrosopumilus maritimus* and their implications for archaeal lipid distributions in the marine environment. *Geochimica et Cosmochimica Acta*, *141*, 579–597. <https://doi.org/10.1016/j.gca.2014.07.005>
- Elling, F. J., Könneke, M., Mußmann, M., Greve, A., & Hinrichs, K.-U. (2015). Influence of temperature, pH, and salinity on membrane lipid composition and TEX₈₆ of marine planktonic thaumarchaeal isolates. *Geochimica et Cosmochimica Acta*, *171*, 238–255. <https://doi.org/10.1016/j.gca.2015.09.004>
- Elling, F. J., Könneke, M., Nicol, G. W., Stieglmeier, M., Bayer, B., Spieck, E., et al. (2017). Chemotaxonomic characterisation of the thaumarchaeal lipidome. *Environmental Microbiology*, *19*(7), 2681–2700. <https://doi.org/10.1111/1462-2920.13759>
- Emeis, K.-C., Schulz, H., Struck, U., Rossignol-Strick, M., Erlenkeuser, H., Howell, M. W., et al. (2003). Eastern Mediterranean surface water temperatures and δ¹⁸O composition during deposition of sapropels in the late Quaternary. *Paleoceanography*, *18*(1), 1005. <https://doi.org/10.1029/2000PA000617>
- Essallami, L., Sicre, M.-A., Kallel, N., Labeyrie, L., & Siani, G. (2007). Hydrological changes in the Mediterranean Sea over the last 30,000 years. *Geochemistry, Geophysics, Geosystems*, *8*, Q07002. <https://doi.org/10.1029/2007GC001587>
- Frigola, J., Canals, M., Cacho, I., Moreno, A., Sierro, F. J., Flores, J. A., et al. (2012). A 500 kyr record of global sea-level oscillations in the Gulf of Lion, Mediterranean Sea: New insights into MIS 3 sea-level variability. *Climate of the Past*, *8*(3), 1067–1077. <https://doi.org/10.5194/cp-8-1067-2012>
- Galand, P. E., Gutiérrez-Provecho, C., Massana, R., Gasol, J. M., & Casamayor, E. O. (2010). Inter-annual recurrence of archaeal assemblages in the coastal NW Mediterranean Sea (Blanes Bay Microbial Observatory). *Limnology and Oceanography*, *55*(5), 2117–2125. <https://doi.org/10.4319/lo.2010.55.5.2117>
- Gent, P. R., Danabasoglu, G., Donner, L. J., Holland, M. M., Hunke, E. C., Jayne, S. R., et al. (2011). The community climate system model Version 4. *Journal of Climate*, *24*(19), 4973–4991. <https://doi.org/10.1175/2011JCLI4083.1>
- Giorgetta, M. A., Jungclaus, J., Reick, C. H., Legutke, S., Bader, J., Böttinger, M., et al. (2013). Climate and carbon cycle changes from 1850 to 2100 in MPI-ESM simulations for the Coupled Model Intercomparison Project phase 5. *Journal of Advances in Modeling Earth Systems*, *5*, 572–597. <https://doi.org/10.1002/jame.20038>
- Harrison, S. P., Bartlein, P. J., & Prentice, I. C. (2016). What have we learnt from palaeoclimate simulations? *Journal of Quaternary Science*, *31*(4), 363–385. <https://doi.org/10.1002/jqs.2842>
- Hayes, A., Kucera, M., Kallel, N., Sbaifi, L., & Rohling, E. J. (2005). Glacial Mediterranean Sea surface temperatures based on planktonic foraminiferal assemblages. *Quaternary Science Reviews*, *24*(7–9), 999–1016. <https://doi.org/10.1016/j.quascirev.2004.02.018>
- Ho, S. L., Mollenhauer, G., Fietz, S., Martínez-García, A., Lamy, F., Rueda, G., et al. (2014). Appraisal of TEX₈₆ and TEX₈₆^L thermometries in subpolar and polar regions. *Geochimica et Cosmochimica Acta*, *131*, 213–226. <https://doi.org/10.1016/j.gca.2014.01.001>
- Hopmans, E. C., Schouten, S., & Sinninghe Damsté, J. S. (2016). The effect of improved chromatography on GDGT-based palaeoproxies. *Organic Geochemistry*, *93*, 1–6. <https://doi.org/10.1016/j.orggeochem.2015.12.006>
- Hopmans, E. C., Weijers, J. W. H., Schefuß, E., Herfort, L., Sinninghe Damsté, J. S., & Schouten, S. (2004). A novel proxy for terrestrial organic matter in sediments based on branched and isoprenoid tetraether lipids. *Earth and Planetary Science Letters*, *224*(1–2), 107–116. <https://doi.org/10.1016/j.epsl.2004.05.012>
- Hossain, A., Zhang, X., & Lohmann, G. (2018). A model-data comparison of the Last Glacial Maximum surface temperature changes. *Climate of the Past Discussions*, *2018*, 1–18. <https://doi.org/10.5194/cp-2018-9>
- Huguet, C., Hopmans, E. C., Febo-Ayala, W., Thompson, D. H., Sinninghe Damsté, J. S., & Schouten, S. (2006). An improved method to determine the absolute abundance of glycerol dibiphytanyl glycerol tetraether lipids. *Organic Geochemistry*, *37*(9), 1036–1041. <https://doi.org/10.1016/j.orggeochem.2006.05.008>
- Huguet, C., Schimmelmann, A., Thunell, R., Lourens, L. J., Sinninghe Damsté, J. S., & Schouten, S. (2007). A study of the TEX₈₆ paleothermometer in the water column and sediments of the Santa Barbara Basin, California. *Paleoceanography*, *22*, PA3203. <https://doi.org/10.1029/2006PA001310>
- Izumi, K., Bartlein, P. J., & Harrison, S. P. (2013). Consistent large-scale temperature responses in warm and cold climates. *Geophysical Research Letters*, *40*, 1817–1823. <https://doi.org/10.1002/grl.50350>
- Jiménez-Amat, P., & Zahn, R. (2015). Offset timing of climate oscillations during the last two glacial-interglacial transitions connected with large-scale freshwater perturbation. *Paleoceanography*, *30*, 768–788. <https://doi.org/10.1002/2014PA002710>
- Kaiser, J., Ruggieri, N., Hefter, J., Siegel, H., Mollenhauer, G., Arz, H. W., & Lamy, F. (2014). Lipid biomarkers in surface sediments from the Gulf of Genoa, Ligurian sea (NW Mediterranean Sea) and their potential for the reconstruction of palaeo-environments. *Deep Sea Research Part I: Oceanographic Research Papers*, *89*, 68–83. <https://doi.org/10.1016/j.dsr.2014.04.009>
- Kallel, N., Duplessy, J.-C., Labeyrie, L., Fontugne, M., Paterne, M., & Montacer, M. (2000). Mediterranean pluvial periods and sapropel formation over the last 200 000 years. *Palaeogeography, Palaeoclimatology, Palaeoecology*, *157*(1–2), 45–58. [https://doi.org/10.1016/S0031-0182\(99\)00149-2](https://doi.org/10.1016/S0031-0182(99)00149-2)
- Kallel, N., Paterne, M., Labeyrie, L., Duplessy, J.-C., & Arnold, M. (1997). Temperature and salinity records of the Tyrrhenian Sea during the last 18,000 years. *Palaeogeography, Palaeoclimatology, Palaeoecology*, *135*(1), 97–108. [https://doi.org/10.1016/S0031-0182\(97\)00021-7](https://doi.org/10.1016/S0031-0182(97)00021-7)
- Kandiano, E. S., Bauch, H. A., & Fahl, K. (2014). Last interglacial surface water structure in the western Mediterranean (Balearic) Sea: Climatic variability and link between low and high latitudes. *Global and Planetary Change*, *123*, 67–76. <https://doi.org/10.1016/j.gloplacha.2014.10.004>
- Kang, S., Shin, K.-H., & Kim, J.-H. (2017). Occurrence and distribution of hydroxylated isoprenoid glycerol dialkyl glycerol tetraethers (OH-GDGTs) in the Han River system, South Korea. *Acta Geochimica*, *36*(3), 367–369. <https://doi.org/10.1007/s11631-017-0165-3>

- Kim, J.-H., Crosta, X., Michel, E., Schouten, S., Duprat, J., & Sinninghe Damsté, J. S. (2009). Impact of lateral transport on organic proxies in the Southern Ocean. *Quaternary Research*, *71*(2), 246–250. <https://doi.org/10.1016/j.yqres.2008.10.005>
- Kim, J.-H., Schouten, S., Rodrigo-Gámiz, M., Rampen, S., Marino, G., Huguet, C., et al. (2015). Influence of deep-water derived isoprenoid tetraether lipids on the TEX₈₆^H paleothermometer in the Mediterranean Sea. *Geochimica et Cosmochimica Acta*, *150*, 125–141. <https://doi.org/10.1016/j.gca.2014.11.017>
- Kim, J.-H., van der Meer, J., Schouten, S., Helmke, P., Willmott, V., Sangiorgi, F., et al. (2010). New indices and calibrations derived from the distribution of crenarchaeal isoprenoid tetraether lipids: Implications for past sea surface temperature reconstructions. *Geochimica et Cosmochimica Acta*, *74*(16), 4639–4654. <https://doi.org/10.1016/j.gca.2010.05.027>
- Kim, J.-H., Villanueva, L., Zell, C., & Sinninghe Damsté, J. S. (2016). Biological source and provenance of deep-water derived isoprenoid tetraether lipids along the Portuguese continental margin. *Geochimica et Cosmochimica Acta*, *172*, 177–204. <https://doi.org/10.1016/j.gca.2015.09.010>
- Kremer, A., Stein, R., Fahl, K., Ji, Z., Yang, Z., Wiers, S., et al. (2018). Changes in sea ice cover and ice sheet extent at the Yermak Plateau during the last 160 ka—Reconstructions from biomarker records. *Quaternary Science Reviews*, *182*, 93–108. <https://doi.org/10.1016/j.quascirev.2017.12.016>
- Kucera, M., Rosell-Melé, A., Schneider, R., Waelbroeck, C., & Weinelt, M. (2005). Multiproxy approach for the reconstruction of the glacial ocean surface (MARGO). *Quaternary Science Reviews*, *24*(7–9), 813–819. <https://doi.org/10.1016/j.quascirev.2004.07.017>
- Lee, K. E., Kim, J.-H., Wilke, I., Helmke, P., & Schouten, S. (2008). A study of the alkenone, TEX₈₆, and planktonic foraminifera in the Benguela Upwelling System: implications for past sea surface temperature estimates. *Geochemistry, Geophysics, Geosystems*, *9*, Q10019. <https://doi.org/10.1029/2008GC002056>
- Leider, A., Hinrichs, K.-U., Mollenhauer, G., & Versteegh, G. J. M. (2010). Core-top calibration of the lipid-based U^{K'}₃₇ and TEX₈₆ temperature proxies on the southern Italian shelf (SW Adriatic Sea, Gulf of Taranto). *Earth and Planetary Science Letters*, *300*(1), 112–124. <https://doi.org/10.1016/j.epsl.2010.09.042>
- Li, L., Lin, P., Yu, Y., Wang, B., Zhou, T., Liu, L., et al. (2013). The flexible global ocean-atmosphere-land system model, grid-point version 2: FGOALS-g2. *Advances in Atmospheric Sciences*, *30*(3), 543–560. <https://doi.org/10.1007/s00376-012-2140-6>
- Lisiecki, L. E., & Raymo, M. E. (2005). A Pliocene-Pleistocene stack of 57 globally distributed benthic δ¹⁸O records. *Paleoceanography*, *20*, PA1003. <https://doi.org/10.1029/2004PA001071>
- Liu, X.-L., Lipp, J. S., Simpson, J. H., Lin, Y.-S., Summons, R. E., & Hinrichs, K.-U. (2012). Mono- and dihydroxyl glycerol dibiphytanyl glycerol tetraethers in marine sediments: Identification of both core and intact polar lipid forms. *Geochimica et Cosmochimica Acta*, *89*, 102–115. <https://doi.org/10.1016/j.gca.2012.04.053>
- Locarnini, R. A., Mishonov, A. V., Antonov, J. I., Boyer, T. P., Garcia, H. E., Baranova, O. K., et al. (2013). World Ocean Atlas 2013, volume 1: Temperature. S. Levitus, (Ed.), A. Mishonov, (Technical Ed.), NOAA Atlas NESDIS 73 (p. 40). Silver Spring, MD: National Oceanographic Data Center. Retrieved from <https://www.nodc.noaa.gov/OC5/indprod.html>
- Lü, X., Chen, J., Han, T., Yang, H., Wu, W., Ding, W., & Hinrichs, K.-U. (2019). Origin of hydroxyl GDGTs and regular isoprenoid GDGTs in suspended particulate matter of Yangtze River Estuary. *Organic Geochemistry*, *128*, 78–85. <https://doi.org/10.1016/j.orggeochem.2018.12.010>
- Lü, X., Liu, X. L., Elling, F. J., Yang, H., Xie, S., Song, J., et al. (2015). Hydroxylated isoprenoid GDGTs in Chinese coastal seas and their potential as a paleotemperature proxy for mid-to-low latitude marginal seas. *Organic Geochemistry*, *89–90*, 31–43. <https://doi.org/10.1016/j.orggeochem.2015.10.004>
- MARGO Project Members (2009). Constraints on the magnitude and patterns of ocean cooling at the Last Glacial Maximum. *Nature Geoscience*, *2*(2), 127–132. <https://doi.org/10.1038/ngeo411>
- Martrat, B., Grimalt, J. O., Lopez-Martinez, C., Cacho, I., Sierro, F. J., Flores, J. A., et al. (2004). Abrupt temperature changes in the Western Mediterranean over the past 250,000 years. *Science*, *306*(5702), 1762–1765. <https://doi.org/10.1126/science.1101706>
- Martrat, B., Grimalt, J. O., Shackleton, N. J., de Abreu, L., Hutterli, M. A., & Stocker, T. F. (2007). Four climate cycles of recurring deep and surface water destabilizations on the Iberian Margin. *Science*, *317*(5837), 502–507. <https://doi.org/10.1126/science.1139994>
- Martrat, B., Grimalt, J. O., Villanueva, J., van Krevelend, S., & Sarnthein, M. (2003). Climatic dependence of the organic matter contributions in the north eastern Norwegian Sea over the last 15,000 years. *Organic Geochemistry*, *34*(8), 1057–1070. [https://doi.org/10.1016/S0146-6380\(03\)00084-6](https://doi.org/10.1016/S0146-6380(03)00084-6)
- Martrat, B., Jiménez-Amat, P., Zahn, R., & Grimalt, J. O. (2014). Similarities and dissimilarities between the last two deglaciations and interglaciations in the North Atlantic region. *Quaternary Science Reviews*, *99*, 122–134. <https://doi.org/10.1016/j.quascirev.2014.06.016>
- Masson-Delmotte, V., Kageyama, M., Braconnot, P., Charbit, S., Krinner, G., Ritz, C., et al. (2006a). Past and future polar amplification of climate change: Climate model intercomparisons and ice-core constraints. *Climate Dynamics*, *26*(5), 513–529. <https://doi.org/10.1007/s00382-005-0081-9>
- Masson-Delmotte, V., Kageyama, M., Braconnot, P., Charbit, S., Krinner, G., Ritz, C., et al. (2006b). Past and future polar amplification of climate change: climate model intercomparisons and ice-core constraints. *Climate Dynamics*, *27*(4), 437–440. <https://doi.org/10.1007/s00382-006-0149-1>
- MEDOC GROUP (1970). Observation of formation of deep water in the Mediterranean Sea, 1969. *Nature*, *227*(5262), 1037–1040. <https://doi.org/10.1038/2271037a0>
- Melki, T., Kallel, N., Jorissen, F. J., Guichard, F., Dennielou, B., Berné, S., et al. (2009). Abrupt climate change, sea surface salinity and paleoproductivity in the western Mediterranean Sea (Gulf of Lion) during the last 28 kyr. *Palaeogeography, Palaeoclimatology, Palaeoecology*, *279*(1–2), 96–113. <https://doi.org/10.1016/j.palaeo.2009.05.005>
- Meyers, S. R. (2014). Astrochron: An R package for astrochronology. Retrieved from <https://cran.r-project.org/package=astrochron>
- Millot, C. (1990). The Gulf of Lions' hydrodynamics. *Continental Shelf Research*, *10*(9–11), 885–894. [https://doi.org/10.1016/0278-4343\(90\)90065-T](https://doi.org/10.1016/0278-4343(90)90065-T)
- Monaco, A., Courp, T., Heussner, S., Carbonne, J., Fowler, S. W., & Deniaux, B. (1990). Seasonality and composition of particulate fluxes during ECOMARGE—I, Western Gulf of Lions. *Continental Shelf Research*, *10*(9–11), 959–987. [https://doi.org/10.1016/0278-4343\(90\)90070-3](https://doi.org/10.1016/0278-4343(90)90070-3)
- Müller, P. J., Kirst, G., Ruhland, G., von Storch, I., & Rosell-Melé, A. (1998). Calibration of the alkenone paleotemperature index U^{K'}₃₇ based on core-tops from the eastern South Atlantic and the global ocean (60°N–60°S). *Geochimica et Cosmochimica Acta*, *62*(10), 1757–1772. [https://doi.org/10.1016/S0016-7037\(98\)00097-0](https://doi.org/10.1016/S0016-7037(98)00097-0)
- North Greenland Ice Core Project members (2004). High-resolution record of Northern Hemisphere climate extending into the last interglacial period. *Nature*, *431*(7005), 147–151. <https://doi.org/10.1038/nature02805>

- Pailler, D., & Bard, E. (2002). High frequency palaeoceanographic changes during the past 140 000 yr recorded by the organic matter in sediments of the Iberian Margin. *Paleoceanography, Palaeoclimatology, Palaeoecology*, *181*(4), 431–452. [https://doi.org/10.1016/S0031-0182\(01\)00444-8](https://doi.org/10.1016/S0031-0182(01)00444-8)
- Pasquier, V., Sansjofre, P., Rabineau, M., Révillon, S., Houghton, J., & Fike, D. A. (2017). Pyrite sulfur isotopes reveal glacial–interglacial environmental changes. *Proceedings of the National Academy of Sciences of the United States of America*, *114*(23), 5941–5945. <https://doi.org/10.1073/pnas.1618245114>
- Pasquier, V., Toucanne, S., Sansjofre, P., Dixit, Y., Révillon, S., Mokeddem, Z., & Rabineau, M. (2019). Organic matter isotopes reveal enhanced rainfall activity in Northwestern Mediterranean borderland during warm substages of the last 200 kyr. *Quaternary Science Reviews*, *205*, 182–192. <https://doi.org/10.1016/j.quascirev.2018.12.007>
- Pérez-Folgado, M., Sierro, F. J., Flores, J. A., Cacho, I., Grimalt, J. O., Zahn, R., & Shackleton, N. J. (2003). Western Mediterranean planktonic foraminifera events and millennial climatic variability during the last 70 kyr. *Marine Micropaleontology*, *48*(1–2), 49–70. [https://doi.org/10.1016/S0377-8398\(02\)00160-3](https://doi.org/10.1016/S0377-8398(02)00160-3)
- Pérez-Folgado, M., Sierro, F. J., Flores, J. A., Grimalt, J. O., & Zahn, R. (2004). Paleoclimatic variations in foraminifer assemblages from the Alboran Sea (Western Mediterranean) during the last 150 ka in ODP Site 977. *Marine Geology*, *212*(1–4), 113–131. <https://doi.org/10.1016/j.margeo.2004.08.002>
- Pinardi, N., & Masetti, E. (2000). Variability of the large scale general circulation of the Mediterranean Sea from observations and modelling: A review. *Paleoceanography, Palaeoclimatology, Palaeoecology*, *158*(3–4), 153–173. [https://doi.org/10.1016/S0031-0182\(00\)00048-1](https://doi.org/10.1016/S0031-0182(00)00048-1)
- Prahl, F. G., Sparrow, M. A., & Wolfe, G. V. (2003). Physiological impacts on alkenone paleothermometry. *Paleoceanography*, *18*(2), 1025. <https://doi.org/10.1029/2002PA000803>
- Prahl, F. G., & Wakeham, S. G. (1987). Calibration of unsaturation patterns in long-chain ketone compositions for palaeotemperature assessment. *Nature*, *330*(6146), 367–369. <https://doi.org/10.1038/330367a0>
- R Core Team (2019). *R: A language and environment for statistical computing*. R Foundation for Statistical Computing, Vienna, Austria. <http://www.r-project.org>. Retrieved from <http://www.r-project.org>
- Railsback, L. B., Gibbard, P. L., Head, M. J., Voarintsoa, N. R. G., & Toucanne, S. (2015). An optimized scheme of lettered marine isotope substages for the last 1.0 million years, and the climatostratigraphic nature of isotope stages and substages. *Quaternary Science Reviews*, *111*, 94–106. <https://doi.org/10.1016/j.quascirev.2015.01.012>
- Rama-Corredor, O., Cortina, A., Martrat, B., Lopez, J. F., & Grimalt, J. O. (2018). Removal of bias in C₃₇ alkenone-based sea surface temperature measurements by high-performance liquid chromatography fractionation. *Journal of Chromatography A*, *1567*, 90–98. <https://doi.org/10.1016/j.chroma.2018.07.004>
- Rasmussen, S. O., Andersen, K. K., Svensson, A. M., Steffensen, J. P., Vinther, B. M., Clausen, H. B., et al. (2006). A new Greenland ice core chronology for the last glacial termination. *Journal of Geophysical Research*, *111*, D06102. <https://doi.org/10.1029/2005JD006079>
- Rigual-Hernández, A. S., Bárcena, M. A., Jordan, R. W., Sierro, F. J., Flores, J. A., Meier, K. J. S., et al. (2013). Diatom fluxes in the NW Mediterranean: evidence from a 12-year sediment trap record and surficial sediments. *Journal of Plankton Research*, *35*(5), 1109–1125. <https://doi.org/10.1093/plankt/fbt055>
- Rontani, J.-F., Volkman, J. K., Prahl, F. G., & Wakeham, S. G. (2013). Biotic and abiotic degradation of alkenones and implications for U^{K'}₃₇ paleoproxy applications: A review. *Organic Geochemistry*, *59*, 95–113. <https://doi.org/10.1016/j.orggeochem.2013.04.005>
- Rosell-Melé, A., & Prahl, F. G. (2013). Seasonality of U^{K'}₃₇ temperature estimates as inferred from sediment trap data. *Quaternary Science Reviews*, *72*, 128–136. <https://doi.org/10.1016/j.quascirev.2013.04.017>
- Rouis-Zargouni, I., Turon, J.-L., Londeix, L., Essallami, L., Kallel, N., & Sicre, M.-A. (2010). Environmental and climatic changes in the central Mediterranean Sea (Siculo-Tunisian Strait) during the last 30 ka based on dinoflagellate cyst and planktonic foraminifera assemblages. *Paleoceanography, Palaeoclimatology, Palaeoecology*, *285*(1–2), 17–29. <https://doi.org/10.1016/j.palaeo.2009.10.015>
- Sánchez Goñi, M. F., Landais, A., Fletcher, W. J., Naughton, F., Desprat, S., & Duprat, J. (2008). Contrasting impacts of Dansgaard-Oeschger events over a western European latitudinal transect modulated by orbital parameters. *Quaternary Science Reviews*, *27*(11–12), 1136–1151. <https://doi.org/10.1016/j.quascirev.2008.03.003>
- Sanchi, L., Ménot, G., & Bard, E. (2013). An automated purification method for archaeal and bacterial tetraethers in soils and sediments. *Organic Geochemistry*, *54*, 83–90. <https://doi.org/10.1016/j.orggeochem.2012.10.005>
- Sbaffi, L., Wezel, F. C., Kallel, N., Paterne, M., Cacho, I., Ziveri, P., & Shackleton, N. J. (2001). Response of the pelagic environment to palaeoclimatic changes in the central Mediterranean Sea during the Late Quaternary. *Marine Geology*, *178*(1–4), 39–62. [https://doi.org/10.1016/S0025-3227\(01\)00185-2](https://doi.org/10.1016/S0025-3227(01)00185-2)
- Schmidt, G. A., Annan, J. D., Bartlein, P. J., Cook, B. I., Guilyardi, E., Hargreaves, J. C., et al. (2014). Using palaeo-climate comparisons to constrain future projections in CMIP5. *Climate of the Past*, *10*(1), 221–250. <https://doi.org/10.5194/cp-10-221-2014>
- Schouten, S., Hopmans, E. C., Schefuß, E., & Sinninghe Damsté, J. S. (2002). Distributional variations in marine crenarchaeotal membrane lipids: A new tool for reconstructing ancient sea water temperatures? *Earth and Planetary Science Letters*, *204*(1–2), 265–274. [https://doi.org/10.1016/S0012-821X\(02\)00979-2](https://doi.org/10.1016/S0012-821X(02)00979-2)
- Schouten, S., Hopmans, E. C., & Sinninghe Damsté, J. S. (2013). The organic geochemistry of glycerol dialkyl glycerol tetraether lipids: A review. *Organic Geochemistry*, *54*, 19–61. <https://doi.org/10.1016/j.orggeochem.2012.09.006>
- Schmidt, G. A., Kelley, M., Nazarenko, L., Ruedy, R., Russell, G. L., Aleinov, I., et al. (2014). *Journal of Advances in Modeling Earth Systems*, *6*, 141–184. <https://doi.org/10.1002/2013MS000265>
- Sicre, M.-A., Siani, G., Genty, D., Kallel, N., & Essallami, L. (2013). Seemingly divergent sea surface temperature proxy records in the central Mediterranean during the last deglaciation. *Climate of the Past*, *9*(3), 1375–1383. <https://doi.org/10.5194/cp-9-1375-2013>
- Sicre, M.-A., Ternois, Y., Miquel, J.-C., & Marty, J.-C. (1999). Alkenones in the northwestern Mediterranean Sea: Interannual variability and vertical transfer. *Geophysical Research Letters*, *26*(12), 1735–1738. <https://doi.org/10.1029/1999GL900353>
- Sierro, F. J., Andersen, N., Bassetti, M. A., Berné, S., Canals, M., Curtis, J. H., et al. (2009). Phase relationship between sea level and abrupt climate change. *Quaternary Science Reviews*, *28*(25–26), 2867–2881. <https://doi.org/10.1016/j.quascirev.2009.07.019>
- Sikes, E. L., O'Leary, T., Nodder, S. D., & Volkman, J. K. (2005). Alkenone temperature records and biomarker flux at the subtropical front on the Chatham Rise, SW Pacific Ocean. *Deep Sea Research Part I: Oceanographic Research Papers*, *52*(5), 721–748. <https://doi.org/10.1016/j.dsr.2004.12.003>
- Sinninghe Damsté, J. S., Rijpstra, W. I. C., Hopmans, E. C., Jung, M. Y., Kim, J. G., Rhee, S. K., et al. (2012). Intact polar and core glycerol dibiphytanyl glycerol tetraether lipids of Group I.1a and I.1b *Thaumarchaeota* in soil. *Applied and Environmental Microbiology*, *78*(19), 6866–6874. <https://doi.org/10.1128/AEM.01681-12>
- Svensson, A., Andersen, K. K., Bigler, M., Clausen, H. B., Dahl-Jensen, D., Davies, S. M., et al. (2008). A 60 000 year Greenland stratigraphic ice core chronology. *Climate of the Past*, *4*(1), 47–57. <https://doi.org/10.5194/cp-4-47-2008>

- Taylor, K. W. R., Huber, M., Hollis, C. J., Hernandez-Sanchez, M. T., & Pancost, R. D. (2013). Re-evaluating modern and Palaeogene GDGT distributions: Implications for SST reconstructions. *Global and Planetary Change*, *108*, 158–174. <https://doi.org/10.1016/j.gloplacha.2013.06.011>
- Ternois, Y., Sicre, M.-A., Boireau, A., Conte, M. H., & Eglinton, G. (1997). Evaluation of long-chain alkenones as paleo-temperature indicators in the Mediterranean Sea. *Deep Sea Research Part I: Oceanographic Research Papers*, *44*(2), 271–286. [https://doi.org/10.1016/S0967-0637\(97\)89915-3](https://doi.org/10.1016/S0967-0637(97)89915-3)
- Ternois, Y., Sicre, M.-A., Boireau, A., Marty, J.-C., & Miquel, J.-C. (1996). Production pattern of alkenones in the Mediterranean Sea. *Geophysical Research Letters*, *23*(22), 3171–3174. <https://doi.org/10.1029/96GL02910>
- Tierney, J. E., & Tingley, M. P. (2014). A Bayesian, spatially-varying calibration model for the TEX₈₆ proxy. *Geochimica et Cosmochimica Acta*, *127*, 83–106. <https://doi.org/10.1016/j.gca.2013.11.026>
- Tierney, J. E., & Tingley, M. P. (2015). A TEX₈₆ surface sediment database and extended Bayesian calibration. *Scientific Data*, *2*, 150029. <https://doi.org/10.1038/sdata.2015.29>
- Tierney, J. E., & Tingley, M. P. (2018). BAYSPLINE: A new calibration for the alkenone paleothermometer. *Paleoceanography and Paleoclimatology*, *33*, 281–301. <https://doi.org/10.1002/2017PA003201>
- Voldoire, A., Sanchez-Gomez, E., Salas y Méria, D., Decharme, B., Cassou, C., Sénési, S., et al. (2013). The CNRM-CM5.1 global climate model: Description and basic evaluation. *Climate Dynamics*, *40*(9–10), 2091–2121. <https://doi.org/10.1007/s00382-011-1259-y>
- Watanabe, S., Hajima, T., Sudo, K., Nagashima, T., Takemura, T., Okajima, H., et al. (2011). MIROC-ESM 2010: Model description and basic results of CMIP5-20c3m experiments. *Geoscientific Model Development*, *4*(4), 845–872. <https://doi.org/10.5194/gmd-4-845-2011>
- Weijers, J. W. H., Schouten, S., Spaargaren, O. C., & Sinninghe Damsté, J. S. (2006). Occurrence and distribution of tetraether membrane lipids in soils: Implications for the use of the TEX₈₆ proxy and the BIT index. *Organic Geochemistry*, *37*(12), 1680–1693. <https://doi.org/10.1016/j.orggeochem.2006.07.018>
- Xing, L., Sachs, J. P., Gao, W., Tao, S., Zhao, X., Li, L., et al. (2015). TEX₈₆ paleothermometer as an indication of bottom water temperature in the Yellow Sea. *Organic Geochemistry*, *86*, 19–31. <https://doi.org/10.1016/j.orggeochem.2015.05.007>
- Yang, H., Xiao, W., Slowakiewicz, M., Ding, W., Ayari, A., Dang, X., & Pei, H. (2019). Depth-dependent variation of archaeal ether lipids along soil and peat profiles from southern China: Implications for the use of isoprenoidal GDGTs as environmental tracers. *Organic Geochemistry*, *128*, 42–56. <https://doi.org/10.1016/j.orggeochem.2018.12.009>
- Yang, Y., Gao, C., Dang, X., Ruan, X., Lü, X., Xie, S., et al. (2018). Assessing hydroxylated isoprenoid GDGTs as a paleothermometer for the tropical South China Sea. *Organic Geochemistry*, *115*, 156–165. <https://doi.org/10.1016/j.orggeochem.2017.10.014>
- Yukimoto, S., Adachi, Y., Hosaka, M., Sakami, T., Yoshimura, H., Hirabara, M., et al. (2012). A new global climate model of the Meteorological Research Institute: MRI-CGCM3—Model description and basic performance. *Journal of the Meteorological Society of Japan. Series II, 90A*, 23–64. <https://doi.org/10.2151/jmsj.2012-A02>
- Zhang, Y. G., & Liu, X. (2018). Export depth of the TEX₈₆ signal. *Paleoceanography and Paleoclimatology*, *33*, 666–671. <https://doi.org/10.1029/2018PA003337>
- Zhang, Y. G., Pagani, M., & Wang, Z. (2016). Ring Index: A new strategy to evaluate the integrity of TEX₈₆ paleothermometry. *Paleoceanography*, *31*, 220–232. <https://doi.org/10.1002/2015PA002848>
- Zhang, Y. G., Zhang, C. L., Liu, X.-L., Li, L., Hinrichs, K.-U., & Noakes, J. E. (2011). Methane Index: A tetraether archaeal lipid biomarker indicator for detecting the instability of marine gas hydrates. *Earth and Planetary Science Letters*, *307*(3–4), 525–534. <https://doi.org/10.1016/j.epsl.2011.05.031>
- Zhu, C., Wakeham, S. G., Elling, F. J., Basse, A., Mollenhauer, G., Versteegh, G. J. M., et al. (2016). Stratification of archaeal membrane lipids in the ocean and implications for adaptation and chemotaxonomy of planktonic archaea. *Environmental Microbiology*, *18*(12), 4324–4336. <https://doi.org/10.1111/1462-2920.13289>
- Zickel, M., Becker, D., Verheul, J., Yener, Y., & Willmes, C. (2016). Paleocoastlines GIS dataset. CRC806-Database. <https://doi.org/10.5880/SFB806.20>